Avalanche Photodiode Photon Counting Receivers for Space-borne Lidars

— progress Report on NAG5-356

"Optical Communication with Semiconductor Laser Diode"

for the period March 1990 — February 1991

Xiaoli Sun and *Frederic M. Davidson*

ABSTRACT

Avalanche photodiodes (APD) are studied for use as photon counting detectors in space-borne lidars. Non break-down APD photon counters, in which the APDs are biased below the break-down point, are shown to outperform conventional APD photon counters biased above the break-down point and to outperform APDs in analog mode when the received optical signal is extremely weak. Nonbreak-down APD photon counters were shown experimentally to achieve an effective photon counting quantum efficiency of 5.0% at $\lambda = 820$ nm with a dead time of 15 ns and a dark count rate of 7000/s which agreed with the theoretically predicted values. The interarrival times of the counts followed an exponential distribution and the counting statistics appeared to follow a Poisson distribution with no after pulsing. It is predicted that the effective photon counting quantum efficiency can be improved to 18.7% at $\lambda = 820$ nm and 1.46% at $\lambda = 1060$ nm with a dead time of a few nanoseconds by using more advanced commercially available electronic components.

March 1991

1. Introduction

Space-borne lidar systems have become an important tool for earth science and space explorations. Diode laser pumped Nd:YAG lasers are among the most attractive laser sources for space-borne lidars because of their small size, high output power, high efficiency, high optical beam quality, long lifetime, and inherent system redundancy. Silicon avalanche photodiodes (APD) can provide the highest receiver sensitivity among other types of photodetectors at the fundamental wavelength of Nd:YAG lasers (λ=1060nm). APDs may be used in either analog or photon counting (Geiger) modes. We report here a detailed study of the sensitivities of lidar receivers which use APD photodetectors, especially APDs operated in the photon counting mode, when biased slightly below the break-down voltage. APDs under this operation condition are shown to always outperform APD photon counting receivers biased above the break-down voltage and to outperform APDs in analog mode when the incident light level is extremely low.

Lidars in space have mainly three types of scientific applications: cloud and aerosol ranging [1], atmospheric back light scattering measurement [2], and spacecraft to ground altitude ranging [3]. All these applications require the lidar receivers to measure the reflected light energy integrated over a short time interval. The lidar receivers have to be extremely sensitive and have wide dynamic ranges because of the great distances from the host spacecraft to targets and the possible variation in the reflectivities of targets. Silicon APDs are the photodetectors of the choice at λ=1060nm because of their relatively high quantum efficiencies which are typically 6% [4], but can be as high as 40% [3, p. 468]. As a comparison, the quantum efficiencies of typical photomultiplier tubes (PMT) are only about 0.1% at the this wavelength [5].

APD's are normally operated in either analog or avalanche break-down photon counting modes. In analog mode, an APD is biased slightly below the break-down voltage such that the average output current is linear in the incident optical power and equal to the primary photocurrent multiplied by an internal avalanche gain. In the avalanche break-down photon counting mode, an APD is biased above the break-down voltage such that individual detected photons trigger an avalanche break-down which results in a strong output current spike that can then be individually counted. The performance of APDs in analog mode are limited by the APD excess noise due to the randomness of the APD gain mechanism. On the other hand, APDs in avalanche break-down photon counting mode are subject to after pulsing and a relatively long dead time due to the slow recovery process after each avalanche break-down.

APDs may also be operated in photon counting mode with the bias voltage below the break-down point. The average APD gain in such a photon counter should be set to its highest stable value, which may require APD temperature control and a highly stable bias voltage supply. Each photon absorption will result in a photocurrent pulse but the amplitude of these photocurrent pulses are much smaller than those output by APDs biased above the break-down point. Consequently, a high gain low noise amplifier and discriminator are required to detect these relatively weak photocurrent pulses. The major advantages of this type of photon counter over the break-down APD photon counters are the elimination of both after pulsing and the slow recovery process following each avalanche break-down. As a result, the counter dead times is limited only by the electrical bandwidth of the APD and the subsequent circuits. The major obstacle toward implementation of this type of APD photon counter has been the lack of wide band and low noise APD preamplifiers. Kikuchi and et. al. (1985) first implemented and tested such a nonbreak-down APD photon counter,

in which the APD and preamplifier were held at 77 °K in order to reduce thermal noise [6]. Lightstone and McIntyre (1988) gave a partial characterization of this type of APD photon counter along with some measurement data at room temperature [7]. However, the dead time of their experimental photon counter was rather long (>0.5 μs) because the electrical bandwidth had to be kept relatively small in order to find a preamplifier with sufficiently low thermal noise.

We have developed a complete theoretical model to characterize this type of nonbreak-down APD photon counter. An experimental system was built and tested. The measured data agreed well with the theoretically predicted values. The measured photon counts appeared to have a Poisson distribution and the interarrival times fit an exponential distribution, as expected. The dead time was measured to be about 15 ns, which is the shortest yet reported for APD photon counters operated in either nonbreak-down or break-down mode. The overall photon detection efficiency was about 5.0% at λ=820nm, which projects to about 0.39% at λ=1060nm, based on the typical spectral response curve of silicon APDs [4]. It is predicted that the overall photon detection efficiency can be improved to as high as 18.7% at λ=820nm and 1.46% at λ=1060nm with a dead time of a few nanoseconds by using more advanced electronic components.

The rest of this report is organized as follows. Sections 2 and 3 give brief reviews of APDs in analog and break-down photon counting modes, respectively. Section 4 gives a detailed description and performance analysis of APD photon counters under nonbreak-down operation. The experiments and measurement data are presented in Section 5. Section 6 contains conclusions along with some predicted performance of APDs in nonbreak-down photon counting mode when using more advanced electro-optical and electronics devices.

2. APDs in Analog Mode Operation

When an APD is biased below the break-down voltage, the average output photocurrent is proportional to the incident optical power. The photocurrent in a lidar receiver is usually first integrated and then fed into a microprocessor through an A-D converter. The number of photons received over the integration time can be estimated by dividing the integrated photoelectron charge by the electron charge and the average APD gain. The advantage of APDs over ordinary photodiodes is that the primary photoelectron current in an APD is multiplied by an internal multiplication gain, as in a photomultiplier tube. Since in practice there is always circuit thermal noise present which appears as additive noise in the total APD output photocurrent, the use of an APD can increase the level of the optically generated signal and consequently improve the receiver sensitivities. However, use of an APD also causes an excess noise in the APD output due to the randomness of the APD gain. The excess noise is usually characterized by an excess noise factor defined as $F=E\{m^2\}/(E\{m\})^2$ with m the random multiplication gain of the APD. The excess noise factor is related to the APD device parameters by [8]

$$F = k_{eff}\, G + (2-\frac{1}{G})(1-k_{eff}) \tag{1}$$

where k_{eff} is the ratio of the ionization coefficients of holes and electrons in the multiplication region of the APD, G is the average APD gain which is controlled by the bias voltage. The smallest value of the excess noise factor is two for ideal APDs with $k_{eff} \rightarrow 0$ and $G \rightarrow \infty$.

In practice, the output signal from an APD is still too small to be conveniently used and it must be further amplified for subsequent signal processing. Each amplifier adds thermal noise to the output but the dominate thermal noise source is from the first stage amplifier which is often called the preamplifier.

There are in general two classes of preamplifiers: high input impedance amplifiers and transimpedance amplifiers, as shown in Figures 1 and 2. The former is a high input impedance linear voltage amplifier preceded by an APD load resistor. The latter is a feedback amplifier with the feedback resistor as the APD load resistor.

Figure 1 also shows an equivalent circuit diagram of a high input impedance preamplifier. The bandwidth of the preamplifier can be approximated as inversely proportional to the time constant of the APD load resistance and the total shunt capacitance at the front end of the amplifier. The input shunt capacitance is very difficult to reduce below 1 pF unless the APD and the amplifier are integrated into one chip. The APD load resistance should be as large as possible because the thermal noise current generated by the resistor is inversely proportional to the feedback resistance. In order to achieve low noise and wide bandwidth operation, an equalizer is usually used after the preamplifier to enhance the high frequence response of the entire circuit. The equalizer should, in fact, cancel the pole formed by the input capacitance and the APD load resistance. Since the input capacitance is parasitic and drifts with temperature, a good equalizer is hard to build and the entire circuit may even become unstable. The equalizer also enhances the high frequency noise of the amplifier which becomes dominant as the receiver bandwidth exceeds a certain value. Furthermore, the APD load resistor at the input of the amplifier loads down the bias voltage across the photodetector which may become a major factor in limiting the dynamic range of the receiver. Therefore, high input impedance preamplifiers are not used very often in practice, though they can potentially achieve a higher receiver sensitivity than the other type of preamplifiers [9].

A transimpedance preamplifier is easier to build and more stable in operation. An equivalent circuit of a transimpedance preamplifier is also shown in

Figure 2. The transfer function of the preamplifier can be derived as

$$Z_T(\omega) = \frac{Z_f(\omega)}{1+\frac{1}{A(\omega)}\frac{Z_i(\omega)+Z_f(\omega)}{Z_i(\omega)}}$$

$$\approx Z_f(\omega) = \frac{R_f}{1 + j\omega R_f C_f}, \quad as \quad |A(\omega)| \rightarrow \infty \tag{2}$$

where $Z_f(\omega)$ and $Z_i(\omega)$ are the total input and feedback impedances, $A(\omega)$ is the open loop amplifier gain, and R_f and C_f are the feedback resistance and its parasitic shunt capacitance. As shown in (2), the 3dB bandwidth of a transimpedance amplifier can be approximated as $(2\pi R_f C_f)^{-1}$ Hz. Since the parasitic capacitance across the feedback resistance can be made very small with modern integrated circuit technology, the 3dB bandwidth of a transimpedance amplifier is usually much larger than that of a high input impedance preamplifier with the same value of the APD load resistance. In fact, there is usually no need for an equalizer following the preamplifier. Furthermore, a transimpedance amplifier has little loading effect on the photodetector bias voltage and has a wider dynamic range than a high input impedance preamplifier. Therefore a transimpedance preamplifier is preferred from the overall system performance point of view. The performance analysis in the subsequent sections always assumes that transimpedance preamplifiers are used.

It is convenient to define the received signal as the number of photoelectrons accumulated over the integration time of the lidar receiver. The mean and variance of the signal can be computed as [10]

$$\bar{x} = G\frac{\eta_Q}{hf}(P_s + P_{bg})\tau + \frac{GI_b\tau}{q} + \frac{I_s\tau}{q} \tag{3}$$

and

$$\sigma_x^2 = FG^2\frac{\eta_Q}{hf}(P_s + P_{bg})\tau + FG^2\frac{I_b\tau}{q} + \frac{I_s\tau}{q} + \sigma_{amp}^2 \qquad (4)$$

where η_Q is the quantum efficiency of the APD, hf is the photon energy, P_s and P_{bg} are the received signal and background optical power, τ is the integration time, I_s and I_b are the APD surface and bulk leakage currents, q is the electron charge, and σ_{amp}^2, is the variance of the total amplifier noise equivalent at the input of the preamplifier integrated over τ. Usually, high speed transimpedance preamplifiers have an FET front end and the variance of the total amplifier noise can be expressed as [11][12]

$$\sigma_{amp}^2 = \frac{2KT_a\tau}{q^2R_f} + \frac{I_g\tau}{q} + \frac{E_i}{q^2R_f^2}\tau\left[\frac{1}{2} + (2B_c\tau)\left(\frac{R_f C_i}{\tau}\right)^2\right] \qquad (5)$$

where K is Boltzmann's constant, T_a is the temperature in Kelvin, R_f is the feedback resistance, I_g is the gate leakage current of the FET, E_i is the one sided power spectrum of the series input voltage noise of the amplifier and is given by $E_i = 4KT_a\Gamma/g_m$ with g_m the transconductance of the FET and Γ a numerical factor close to unity, B_c is the cutoff frequency of the integrator, and C_i is the shunt capacitance at the input of amplifier. Theoretically, the frequency response of an ideal integrator is a sinc function, and therefore, the bandwidth required to implement it must be infinite. In practice, the bandwidth is limited to several times the main lobe of the sinc function. It has been shown experimentally [13] that a cutoff frequency of $B_c \geq 2(1/\tau)$ is sufficient for the degradation in performance to be negligible.

The first two terms in (5) are proportional to τ and can be treated as having a constant spectral noise current density (white noise). The last term in (5) corresponds to a spectral noise current density which is proportional to the square of the frequency. Therefore, it is important to keep the parasitic shunt

capacitance at the input of the amplifier as low as possible. For most commercial preamplifiers which have moderate feedback resistance (~KΩ), the power spectrum of the total amplifier noise can be assumed to be constant (white) at least up to a few hundred megahertz. Under this condition, an equivalent noise temperature, $T_e(\,^\circ K)$, can be defined such that the total amplifier noise is equal to the thermal noise generated by the feedback resistance at temperature T_e. The total amplifier noise can then be written, to a good approximation, as

$$\sigma_{amp}^2 \approx \frac{2KT_e\tau}{q^2R_f}. \tag{6}$$

If we define the useful signal as $\bar{x}_s = G(\eta_Q/hf)P_s\tau$, the signal to noise ratio (SNR) of the APD output in analog mode can be written as

$$SNR_{an} = \frac{\bar{x}_s^2}{\sigma_x^2} = \frac{(G\frac{\eta_Q}{hf}P_s\tau)^2}{FG^2\frac{\eta_Q}{hf}(P_s+P_{bg})\tau + FG^2\frac{I_b\tau}{q} + \frac{I_s\tau}{q} + \frac{2KT_e\tau}{q^2R_f}}. \tag{7}$$

There exists an optimal value for the average APD gain which maximizes the SNR_{an}. At the optimal APD gain, the excess noise should be much larger than the amplifier noise. For comparison purposes, we can approximate the SNR_{an} as

$$SNR_{an} \rightarrow \frac{1}{F}\eta_Q\frac{P_s\tau}{hf} = \frac{1}{F}\eta_Q SNR_{QL} \tag{8}$$

where SNR_{QL} is the quantum limited SNR assuming unity quantum efficiency and no amplifier and background radiation noises. Therefore, roughly speaking, the SNR_{an} is a factor of F smaller than that achieved with a photodiode with the same quantum efficiency but no thermal noise and no excess noise. In other words, use of an APD makes the amplifier noise negligible but also causes the signal to noise ratio to decrease roughly by a factor of F. Nevertheless, APDs can significantly improve receiver SNR at λ=1064nm as compared to PMTs

which have little excess noise ($F \approx 1$) but a much lower quantum efficiency. For example, if we assume $F=8.5$, $\eta_{Q_{APD}}=30\%$, and $\eta_{Q_{PMT}}=0.1\%$, the use of an APD can achieve a receiver SNR which is 35 times that of a PMT, except when the optical signal is so weak that the required optimal APD gain is too high to be obtained in practice.

3. APDs under Break-Down Photon Counting Operation

An APD can be biased several volts above its break-down point to achieve photon counting operation [4]. Avalanche break-downs are triggered by both absorbed photons and thermally generated hole-electron pairs inside the device. Each avalanche break-down results in a large current spike which can be easily detected by a discriminator. Figure 3 shows a diagram of a typical APD break-down photon counting circuit [4].

Since not all the received photons can trigger avalanche breakdowns, the average number of photons counted by the discriminator, $\bar{n}_c$, is always less than the average number of absorbed photons, $\bar{n}$. The effective photon counting quantum efficiency can be written as

$$\eta_{Q_{eff}} = \eta_Q \frac{\bar{n}_c}{\bar{n}} = \eta_Q P_{trig} \tag{9}$$

where η_Q is the quantum efficiency of the APD, P_{trig} is the probability that an absorbed photon triggers an avalanche break-down which results in a discriminator threshold crossing. The average number of absorbed photons, $\bar{n}$, over a counting interval, T, is related to the received optical power, P_o, by

$$\bar{n} = \eta_Q P_o T / hf \ . \tag{10}$$

The number of photons being counted, n, should be a Poisson random variable

with mean and variance equal to $\bar{n}_c$. The signal to noise ratio is given by

$$SNR_{ct_0} = \frac{(E\{n\})^2}{var\{n\}} = \bar{n}_c = P_{trig}\,\bar{n} \ . \tag{11}$$

Considering the background noise counts and dark counts, the signal to noise ratio should be

$$SNR_{ct} = \frac{(P_{trig}\,\bar{n}_s)^2}{P_{trig}(\bar{n}_s + \bar{n}_{bg}) + \bar{n}_{dark}} \ . \tag{12}$$

where $\bar{n}_s$ and $\bar{n}_{bg}$ are the average number of absorbed signal and background photons, and $\bar{n}_{dark}$ is the average number of total dark counts caused by the APD dark current and circuit thermal noise.

The probability of triggering, P_{trig}, increases with the bias voltage. However, the number of dark counts triggered by thermally generated hole-electron pairs also increases with the bias voltage. The value of P_{trig} is typically 7% with 15000/sec dark counts at 22 ° C when the APD is biased approximately two volts above the break-down point [4]. Although higher values of P_{trig} (50-80%) can be achieved at even higher bias voltages [14], they cannot be used in lidar receivers because of the excessively high dark count rates and other nonlinear effects. The dark counts can be reduced by cooling the APD. However, the quantum efficiency of the APD may also decrease with temperature over certain wavelength ranges. For example, for a RCA30902S silicon APD, the dark count rate decreases from 15000/sec at 20 ° C to 300/sec at -25 ° C, but the quantum efficiency also decreases by about a factor of two at λ=1064nm [4].

A major disadvantage of break-down type APD photon counters is the existence of so called after pulsing due to excess avalanche break-downs which appear randomly after each avalanche break-down. The cause of after pulsing is attributed to the presence of trapped charges at dislocations and impurities in

the high voltage region of the APD after each avalanche break-down [7]. After pulsings can occur randomly at nanoseconds to kiloseconds after each avalanche break-down but they are mainly distributed within the first a few milliseconds [4][14]. The probability of after pulsing within 1 microsecond to 60 seconds is typically 2-15% [4] and increases with the APD bias voltage. After pulsing is a nonlinear effect and has not been well understood except for some simplified mathematical modeling [15]. In lidar applications, after pulses appear as random echos from the target which reduces the SNR_{ct} or causes confusion in the measurements. Multiple laser firings at one target spot may be required to average out the random echos. In photon correlation spectroscopy measurements, the decay times of the after pulses form a systematic measurement error which sometimes can be overwhelming.

The dead time of a break-down APD photon counter is mainly determined by the recovery process of the APD after each avalanche break-down. Every time a break-down occurs, the APD has to be quenched to prevent any damage to the device. There are two types of quenching circuits: passive quenching and active quenching. One example of passive quenching is shown in Figure 3. When a break-down occurs, the voltage drop across the resistors in series with the APD effectively reduces the APD bias voltage to below the break-down point. The APD bias voltage is then gradually restored as the APD shunt capacitance gets recharged. Since the resistors have to be relatively large to limit the maximum APD current, the recovery process is relatively slow. The typical dead time of this type of photon counter is about one microsecond [4][16]. An active quenching circuit can significantly shorten the dead time by momentarily reducing the resistance in series with the APD upon each break-down so that the APD shunt capacitance can be charged with a much shorter time constant than that of a passive quenching circuit. Brown and et. al. [17] have reported an active

quenching circuit which achieved a dead time of a few tens of nanoseconds.

Because of the existence of a finite dead time, photons which arrive within the dead time cannot be resolved and the number of detected photons is no longer a Poisson random variable. Cantor and Teich [18] have shown that the probability that n' photons are counted over a T second interval in response to $\bar{n}$ average absorbed photons for a given dead time, τ_d, can be written as

$$P_d(n' \,|\bar{n},\tau_d) = \sum_{k=0}^{n'} \frac{[\bar{n}(1-\frac{\tau_d}{T}n')]^k}{k!} e^{-\bar{n}(1-\frac{\tau_d}{T}n')}$$

$$+ \sum_{k=0}^{n'-1} \frac{\{\bar{n}[1-(n'-1)\frac{\tau_d}{T}\}^k}{k!} e^{-\bar{n}[1-(n'-1)\frac{\tau_d}{T}]}, \quad n' < \frac{T}{\tau_d} . \quad (13)$$

The maximum likelihood (ML) estimator, $\hat{n}_{ML}$, of the average number of actually absorbed photons, $\bar{n}$, given n' detected photons under this condition is given by [19]

$$\hat{n}_{ML} = \frac{n'}{1 - n'(\tau_d/T)} . \quad (14)$$

As $\tau_d = 0$, Eq. (13) reduces to a Poisson distribution and Eq. (14) reduces to $\hat{n}_{ML} = n' = n$ which is the actual number of photons being counted. The mean and variance of the ML estimator are given by

$$E\{n\} = var\{n\} = \bar{n} . \quad (15)$$

The signal to noise ratio under this condition is equal to

$$SNR_0 = \frac{(E\{n\})^2}{var\{n\}} = \bar{n}. \quad (16)$$

When $\tau_d \neq 0$, the ML estimator given by (14) become biased and has a larger variance, i.e., $(E\{\hat{n}\}-\bar{n}) \neq 0$ and $var\{\hat{n}\} \geq var\{\hat{n}\}_{\tau_d=0} = \bar{n}$. As a result, the signal

to noise ratio becomes smaller, compared to the ideal case, i.e.

$$SNR(\hat{n}) = \frac{(E\{\hat{n}\})^2}{var\{\hat{n}\}} \leq \frac{(E\{n\})^2}{var\{n\}} = SNR_0 . \tag{17}$$

Figures 4 and 5 show the normalized bias and signal to noise ratio as a function of average number of absorbed photons. It is shown that $(\tau_d / T) \leq 0.01$ is required in order to obtain a reasonably good measurement (i.e. bias$\sim$0 and $SNR(\hat{n}) \sim \bar{n}$. The dead times of avalanche break-down APD photon counters are usually too long for lidar receivers.

4. APDs under Nonbreak-down Photon Counting Operation

APDs may be used to count single photons while being biased below the break-down point as in analog mode [6][7]. The photocurrent pulses resulting from a single photon absorption can be detected via a discriminator threshold crossing with a relatively high probability as long as the APD gain is sufficiently large and the circuit thermal noise is relatively low. There is no after pulsing since the APD is operating in its linear regime. The dead time can also be much shorter than that of a break-down type APD photon counter since the APD bias voltage does not need to be restored after each photon detection. The receiver can be operated in both photon counting and analog modes simultaneously by diverting part of the APD preamplifier output to an analog channel. The analog channel can operate linearly after the photon counting channel is saturated due to a strong input light intensity. Therefore, the dynamic range of the entire receiver can be greatly extended.

4.1. Principle of Operation

The circuit used for this type of photon counter is shown in Figure 6. The APD and preamplifier are exactly the same as those in the analog mode except that the average APD gain is set to the highest achievable value but not necessarily the value which optimizes the output SNR_{an}. This requires some form of APD temperature control or compensation and a very stable bias voltage supply. The output of the preamplifier is compared against a threshold with the use of a comparator or a discriminator whose output is connected to an electrical pulse counter. The threshold level of the discriminator has to be carefully set in order to achieve a high photon detection efficiency while maintaining a tolerable noise count rate. As shown in Figure 6, the dead time of this type of photon counter is limited by the photocurrent pulse width which is about equal to the reciprocal of the bandwidth of the APD and preamplifier. In practice, the dead time is longer than the pulse width because of the limited time resolution of the discriminator and the electrical pulse counter. Since the APD gain is random, the pulse width is a random variable and so is the dead time. The actual dead time distribution usually has to be determined experimentally.

The number of detected signal photon counts and the number of dark counts are both Poisson random variables. The signal to noise ratio can be computed using Eq. (12) by substituting the threshold crossing (discrimination) probability, P_{disc}, for the triggering probability, P_{trig}.

4.2. Effective Quantum Efficiency

Since the APD gain is random, not all the photon absorptions result in photocurrent pulses whose peak amplitudes are large enough to cross the discriminator threshold. The effective quantum efficiency can be written as

$$\eta_{Q_{eff}} = \eta_Q \times \frac{E\{photons\ counted\}}{E\{photons\ absorbed\}} = \eta_Q P_{disc} \tag{18}$$

where η_Q again is the quantum efficiency of the APD and P_{disc} is the probability that a photocurrent pulse in response to a photon absorption is counted. The computation of P_{disc} is given as follows.

Ideally, the photocurrent pulse output from an APD in response to a photon absorption should be an impulse and the preamplifier under this condition can be simplified equivalently to consist of a resistor and a capacitor in parallel. The pulse shape output from the preamplifier is an exponential function as shown in Figure 7 (dotted line). The average area under the pulse shape function is mq with m the instantaneous APD gain and q the electron charge. The peak amplitude of the pulse is given by $i_{phmax}=mq/RC=2\pi GqB_{3dB}$ with B_{3dB} (Hz) the 3 dB bandwidth of the preamplifier. In practice, the APD output cannot be true impulses and the preamplifier is always bandwidth limited. As a result, the shapes of the actual photocurrent pulses output from the APD are not true exponential functions but have a finite rise time, a round peak, and a slower falling edge, as shown in Figure 7 (solid line). Empirically, we choose

$$i_{phmax} = 4mqB_{3dB}, \tag{19}$$

which seems to yield results consistent with the measurements. Equation (19) may have to be modified if the frequency response of the preamplifier or the subsequent circuit is significantly different from that of a RC lowpass filter.

A photon is detected whenever the peak amplitude of a photocurrent pulse exceeds the threshold current, I_{thre}. The probability of discrimination, P_{disc}, is then given by

$$\begin{aligned} P_{disc} &= Prob(i_{phmax} > I_{thre}) = Prob(m \geq M_{thre}) \\ &= \sum_{m=M_{thre}}^{\infty} P(m) \end{aligned} \tag{20}$$

where M_{thre} is the equivalent threshold crossing APD gain given by

$$M_{thre} = \frac{I_{thre}}{4qB_{3dB}} \tag{21}$$

and $P(m)$ is the the probability of the APD gain. McIntyre and Conradi [20][21] have shown that the probability of the APD gain can be written as

$$P(m) = \frac{\Gamma(\frac{m}{1-k_{eff}}+1)}{m!\,\Gamma(\frac{k_{eff}\,m}{1-k_{eff}}+2)} \cdot [\frac{1+k_{eff}\,(G-1)}{G}]^{\frac{k_{eff}\,m}{1-k_{eff}}+1} \cdot [\frac{(1-k_{eff})(G-1)}{G}]^{m-1} \tag{22}$$

with $\Gamma(\cdot)$ the GAMMA function. The equivalent quantum efficiency of this type of photon counter can be evaluated by substituting (21) and (22) into the right hand side of (20).

Figure 8 shows qualitatively the distribution of the APD gain for two different values of the ionization ratios k_{eff} [20]. The probability of discrimination P_{disc} is equal to the shaded area under the curves. It is seen that the smaller the k_{eff}, the larger the P_{disc}. Figure 9 plots P_{disc} as a function of the normalized equivalent threshold crossing APD gain, M_{thre}/G, for G=1200 and k_{eff} =0.010.

4.3. Dark Counts

There are two sources of dark counts: the APD dark current and the circuit thermal noise. The APD dark current consists of surface leakage current and bulk leakage current. The former does not pass through the high gain region of the APD and hardly causes any dark counts. The latter does pass through the high gain region of the APD and acts as a source of background radiation. The number of dark counts due to a bulk leakage current, I_b, can be modeled as a Poisson random variable with the mean equal to

$$\bar{n}_{dark\,1} = P'_{disc}\frac{I_b T}{q} \tag{23}$$

where P'_{disc} is the average probability that an electron of the APD bulk leakage current causes a discriminator threshold crossing. The value of P'_{disc} should be smaller than that for a primary photo electron, i.e. $P'_{disc} < P_{disc}$, since part of the APD bulk leakage current is generated inside the APD high field region and is not multiplied by the full APD gain. We have found experimentally that $P'_{disc} \approx 0.17 P_{disc}$ for a RCA30902S silicon APD which had a bulk leakage current of $I_b \approx 0.1\ pA$

The number of dark counts due to circuit thermal noise should also follow a Poisson distribution if the correlation time of the noise is less than the dead time of the photon counter. The average number of counts due to circuit noise, $\bar{n}_{dark\,2}$, over a counting interval of T seconds can be written as [22]

$$\bar{n}_{dark\,2} = \frac{T}{\overline{\Delta t}} P_{fa} \tag{24}$$

where $\overline{\Delta t}$ is the average threshold crossing time or pulse width which is about equal to the reciprocal of the band width, and P_{fa} is the threshold crossing probability due to the circuit thermal noise at a fixed sampling time. The circuit noise current can be modeled as a zero mean Gaussian random process and the variance can be written similarly to (6) as

$$\sigma^2_{Iamp} = \frac{4KT_e}{R_f} B_n \tag{25}$$

where B_n is the noise bandwidth. If the transimpedance preamplifier can be assumed equivalently as an ideal RC circuit, the noise bandwidth is 1.57 times the 3dB bandwidth [23]. The threshold crossing probability can be expressed as

$$P_{fa} = \int_{I_{thre}}^{\infty} \frac{1}{\sqrt{2\pi\sigma^2_{Iamp}}} e^{-\frac{x^2}{2\sigma^2_{Iamp}}} dx \ . \tag{26}$$

There is always a trade-off between the equivalent quantum efficiency and circuit noise counts. Both P_{disc} and $\bar{n}_{dark2}$ decrease as the threshold I_{thre} increases. Figure 10 shows qualitatively the average number of detected photons, $\bar{n}P_{disc}$, and noise counts, $\bar{n}_{dark2}$, as a function of the threshold current I_{thre}. For best performance, the threshold level should be set at the point where the curve of $\bar{n}_{dark2}$ just starts to level off and the total number of dark counts is much less than that of the photon counts, i.e. $\bar{n}_{dark1} + \bar{n}_{dark2} << \bar{n}P_{disc}$. If the value of the number of absorbed photons, $\bar{n}$, is completely unknown and needs to be determined through the measurement, the threshold level should be set such that the dark counts due to circuit noise are much less than those due to the APD bulk leakage current, i.e. $\bar{n}_{dark2} << \bar{n}_{dark1}$. Usually, the threshold is set to be a few times the standard deviation of the circuit noise, i.e. $I_{thre} = f \times \sigma_{Iamp}$ with f a multiplication factor. The equivalent threshold crossing gain in (21) can be expressed as

$$M_{thre} = \frac{f\,[\frac{4KT_e}{R_f}(1.57B_{3dB})]^{1/2}}{4qB_{3dB}} . \tag{27}$$

The probability of discrimination and the equivalent quantum efficiency can be evaluated by substituting (27) and (22) into (20) and (18). If the photon counter is operating properly, the numbers of detected signal and background photons, the dark counts due to APD leakage current, and the dark counts due to circuit thermal noise should all follow Poisson distributions, and so should the total number of counts.

As seen in (27), the equivalent APD threshold crossing gain M_{thre} is inversely proportional to the square root of the feedback resistance R_f and the 3dB bandwidth of the preamplifier. Since the probability of discrimination P_{disc} increases as M_{thre} decreases, it is important to keep the product of the feedback

resistance and the 3dB bandwidth of the transimpedance preamplifier as large as possible in order to achieve a high photon detection probability.

5. Experiments with Nonbreak-down APD Photon Counters

An experimental nonbreak-down APD photon counter was built and the performance was measured to verify the theoretical model developed in the previous section.

5.1. Experimental Setup

Figure 11 shows the optical setup of the experiment. The light source consisted of an ordinary incandescent light bulb, a diffuser, a pinhole, and a collimating lens. The light bulb was powered by a stable DC voltage supply and the light emitted can be considered to have an almost perfectly constant intensity over a wide spectral range. The light beam was first attenuated and then filtered through two interference filters which were centered at λ=821nm and had a combined bandwidth of $\Delta\lambda$=7nm. The received optical power was measured directly by substituting an optical power meter sensor head for the APD which could be moved aside. The experiment was conducted in total darkness and background radiation could be neglected. A high speed universal counter (Stanford Research SR620, maximum count rate 200×10^6/sec) was used to count the pulses output from the discriminator. The counter also gave the mean, the variance, and histograms of the measured counts.

The details of the electronics are shown in Figure 12. The APD used was a RCA 30902S silicon APD with $k_{eff} = 0.010$, $I_b \approx 0.1\ pA$, and $I_s = 12\ nA$ [13]. The APD preamplifier consisted of a GigaBit Logic 16G071 transimpedance

amplifier (DC-700 MHz, $R_f = 830\ \Omega$ [24]). The signal was further amplified by another two amplifiers to a level which was appropriate (~200 mV) for the discriminator. The attenuators shown in Figure 12 were used to adjust the amplifier gains since there were no other amplifiers in our lab which had just the right gain and dynamic range. A low pass filter was used to block out the high frequency noise and the cutoff frequency (200 MHz) was chosen to correspond to the maximum speed of the discriminator and the counter. The discriminator consisted of a high speed comparator (Motorola MC1650, MECLIII series one bit A/D converter) and the resolution of the comparator was smaller than 20 mV according to the data sheet.

A schematic circuit diagram of the APD/preamplifier DC voltage supply is shown in Figure 13. The high voltage APD bias supply was generated by a DC-DC converter (Analog Modules, Model 521) which had peak output ripples of $<0.003\%$ of the average output DC voltage.

5.2. Circuit Thermal Noise

The total circuit noise at the input of the comparator was measured with a RF power meter (HP-435B with 8482A power sensor head) while biasing the APD about 100 V below its break-down point so that the APD gain was essentially zero and its noise could be neglected. The total RF noise power measured was 2.5 μW over a bandwidth of 0.1-100 MHz. The net gain from the output of the preamplifier to the input of the discriminator was measured to be 46.5$\pm$0.5 dB from 0.1 to 200 MHz with the -3 dB point at 220 MHz. The resultant equivalent noise current at the front end of the transimpedance amplifier was 6.4 pA/$\sqrt{\text{Hz}}$, which was very close to that given by the data sheet (5.7-6.3 pA/$\sqrt{\text{Hz}}$) [24]. Figure 14 shows the power spectrum of the noise measured by a

RF spectrum analyzer (HP-8590A). The spikes in the spectrum were due to electro-magnetic interferences (EMI). The average noise density up to 100 MHz was about -107 dBm/Hz (2.0 μW/100MHz) according to Figure 14 which was close to that measured by the RF power meter (2.5 μW/100MHz) and the discrepancy was believed to be caused by the spikes in the power spectrum. The noise intensity rose by a few dB over the frequency range of 100-200 MHz as shown in Figure 14. The total noise power measured with the RF power meter at the input of the comparator was about 7.0 μW (18.7 mV rms) over the entire bandwidth.

The average noise counts due to the circuit thermal noise were first measured as a function of the absolute value of the threshold level applied at the comparator. The result is shown in Figure 15. The APD was biased well below its break-down point so that the contribution from the APD noise could be neglected. The counting interval was set to one second in this measurement and each point in Figure 15 was based on the average of 100 measurements (sample size). The threshold voltage was measured at the negative input terminal of the comparator with the use of a digital multimeter. The actual threshold voltage was negative since the transimpedance APD preamplifier was an inverting amplifier. It is noticed that the effective threshold level defined in the previous section was higher than that measured at the comparator since the comparator had only limited gain and pulses at the positive input terminal had to exceed the threshold by a certain amount in order to trigger the subsequent counter. For example, the measured threshold voltage was -47.1 mV at a dark count rate of 900 cts/sec and the effective threshold level which corresponded to the same dark count rate should be about 4.5 times the total measured rms circuit thermal noise voltage at the input of the comparator according to (24)-(26), i.e. $V_{effth} = 4.5\times(-18.7mV) = -84.1\ mV$. Therefore, the difference between the measured

and effective threshold levels was about 37 mV in this case.

5.3. Measurements of Photon Counts and Dark Counts

The APD in this measurement was biased as close to the break-down voltage (~252 volt) as possible without an avalanche break-down occurring at any time. An oscilloscope was used to monitor the APD preamplifier output to detect any possible avalanche break-downs which appeared as abnormally large spikes in the output waveform. The actual average APD gain could not be measured directly because the APD was under CW illumination and the amplifiers were AC coupled. However, we had measured the average gain of another APD of the same model number under pulsed illumination and the highest average gain achieved was found to be 1200-1300. Figure 16 shows the average waveforms of input pulses (negative going) and output pulses (positive going) of the comparator. It is noticed that the measured average pulse width (5.857 ns) was only approximated since it depended on the triggering level of the oscilloscope.

The received optical power was adjusted to 1.0 pW. The numbers of total counts and dark counts were measured as a function of the absolute value of the threshold voltage. The means and the standard deviations (error bar) of the measured counts are plotted in Figure 17. The dark counts were measured while blocking the incident light beam. The counting interval was set to 1.0 ms and the sample size was 10,000. The means and standard deviations of the thermal noise counts for the same counting interval and sample size are also shown in Figure 17 (dot-dashed curve). The number of photon counts increased relatively slowly with the threshold level as compared to the dark counts which included the circuit thermal noise counts. At low threshold levels, the circuit thermal noise counts became overwhelming and the standard deviations became

abnormally large, as shown in Figure 17. The optimal threshold should be at the "knee" of the dark counts curve, or between 45 to 50 mV.

Figures 18, 19, and 20 show the histograms of the thermal noise counts, the total dark counts, and the total counts under 1.0 pW received optical power when the threshold level was set to 47.1 mv. The counting interval was set to 1 ms and the sample size was 50,000. The data shown on Figures 18, 19, and 20 are subject to the quantization error of the counter used which only output integers. Theoretically, the numbers of counts should all follow Poisson distributions and the ratio of the variance to the mean should be equal to unity. It was difficult to tell from Figure 18 if the circuit thermal noise counts followed a Poisson distribution since there were too few counts in the 1 ms counting interval. The mean and the standard deviation measured over 1 second were about 900 and 100, respectively. Therefore the distribution of the circuit thermal noise counts was clearly not Poisson. This may be attributed to the fact that the circuit noise was somewhat correlated and the power spectrum was not perfectly flat, as shown in Figure 14. The distributions of the dark counts and total counts under 1.0 pW received optical power appeared to be Poisson within the quantization error of the counter, as shown in Figures 19 and 20.

5.4. Interarrival Times of the Photon Counts

The interarrival times of the observed counts were measured using the apparatus shown in Figure 21. The comparator output was divided into both Channels A and B of the counter which measured the time interval started by a pulse at Channel A and stopped by the next pulse at Channel B. The input at Channel A was delayed by 4.66 ns through a coax cable to avoid the counter being started and stopped by the same pulse. The two channels of the counter

had to be well balanced so that the pulse sequence seen by Channel A was the same as that seen by Channel B.

Figure 22 shows a histogram of the measured interarrival time of the observed total number of counts under 1.0 pW received optical power. The sample size in this measurement was 2×10^5. The heavy solid curve in Figure 22 represents the theoretical values of the exponential distribution of the same mean. The measured interarrival times fit very closely to an exponential distribution. This shows that the performance of the photon counter being tested was very close to that of an ideal photon counter and the detected number of counts follows a Poisson distribution. Figure 23 is a magnification of Figure 22 from 0 to 100 ns. The sharp decrease near the origin was due to the dead time of the photon counter. The fluctuations in the histogram of Figure 22 were due to the finite sample size of the measurements. The average dead time can be approximated as 15 ns after considering the coax cable delay (4.66ns) at Channel A of the counter. Since the dead time was a random number as mentioned in the previous section, the measured interarrival times could occasionally be shorter than the average dead time, as shown in Figure 23.

5.5. Dynamic Range of the Photon Counter

Table 1 shows the mean and standard deviation of the total number of observed counts as a function of the received optical power. The fourth column shows the ratio of the variance to the mean of the measured counts (excluding the effect of the thermal noise counts). It is seen that the detected counts had a near Poisson behavior up to 30 pW received optical power. The circuit seemed to start to saturate as the input optical power exceeded 30 pW. The threshold voltage was set to 47.1 mV so that the total number of dark counts was about

6~7/ms. Table 1 also lists the raw and the dead time corrected equivalent quantum efficiencies (excluding the dark counts). It is shown that the photon counter had a nearly constant equivalent quantum efficiency of about 5.0% for up to 10 pW received optical power or a count rate of about 2000 cts/ms (2,000,000 cts/sec). The total number of counts versus the received optical power, the data in the first and second column of Table 1, are also plotted in Figure 24. The curve tends to level as the received optical power becomes extremely low because dark counts start to dominate. The curve also starts to level off as the received optical power becomes relatively high because of the saturation of the circuit. The center segment of the curve is approximately linear and corresponds to an equivalent quantum efficiency of about 5.0%. This closely agreed with the theoretically predicted value, 6.0% ($P_{disc} = 7.8\%$), according to (20)—(22) assuming that the average APD gain was G=1000, APD quantum efficiency, $\eta = 77\%$, and the effective threshold current level, $I_{thre} = 4.5 \times \sigma_{Iamp}$. The theoretical model given in Section 4 assumes that the frequency response of the entire circuit up to the comparator is the same as that of a RC lowpass filter but the experimental system contained a higher order lowpass filter which had a sharp cutoff frequency. Therefore the actual amplitude of photocurrent pulses might have been smaller than that given by (19). This is believed to be the reason why the theoretically predicted effective quantum efficiency using (19)-(22) is slightly lower than that of the experimental system.

6. Conclusions

We have demonstrated that an APD can be used to count photons while being biased below its break-down point. The major advantages of this type of APD photon counter versus a conventional Geiger mode APD biased above the break-down point are the significantly shorter dead times and the total elimination of after pulsing. A theoretical model has been developed to fully characterize this type of nonbreak-down APD photon counter. The theoretically predicted performance agreed with the experimental measurements. The experimental nonbreak-down APD photon counter achieved an effective quantum efficiency of 5.0% at $\lambda = 820$ nm under a dark count rate of about 7000/second. The counting statistics appeared to follow a Poisson distribution and the interarrival times fit very tightly to an exponential distribution. The measured dead time of the photon counter was about 15 ns and there was no after pulsing observed. The experimental nonbreak-down APD photon counter has already outperformed a typical conventional break-down type of APD photon counter.

The performance of the experimental nonbreak-down photon counter may be further improved just by using more advanced commercially available electronics components. One example is to use a higher speed comparator such as a GaAs device so that the full bandwidth of the APD and preamplifier (700 MHz) can be used. It is assumed that the equivalent threshold current is still 4.5 times the rms noise current so that the dark counts rate is about 7000/second. The APD preamplifier has to be well packaged to eliminate any EMI noise so that the equivalent input noise current meets the specification of the preamplifier ($6pA/\sqrt{Hz}$). The predicted effective quantum efficiency of the photon counter under these condition will be $\eta_{Q_{eff}}$=9.2% at λ=820 nm (η_Q=77%) and $\eta_{Q_{eff}}$=0.72% at λ= 1.06 μm (η=6%) with a dead time of a few nanoseconds.

The linear dynamic range of the photon counter should also be considerably larger due to the shorter dead time. Such a photon counter will be comparable to PMTs at λ = 800 nm and outperform PMTs at λ=1060nm.

The transimpedance APD preamplifier may also be replaced with one which has a higher feedback resistance, for example, GigaBit Logic 16G072 (R_f =30$K\Omega$, B_{3dB}=600 MHz) [24]. The predicted value of P_{disc} under these condition will be 24.3% which corresponds to an effective photon counting quantum efficiency of $\eta_{Q_{eff}}$=18.7% at λ=820 nm and $\eta_{Q_{eff}}$=1.46% at λ= 1.06 μm under the same dark count rate, assuming the average equivalent noise temperature of the preamplifier is T_e = 1500 °K. This photon counter will outperform any PMT at λ > 800 nm and any APD in analog mode with excess noise factor F >4.1.

If we use a state-of-the-art silicon APD [25] in which k_{eff} = 0.005, G = 1000, and η_Q = 90% at λ=820, the predicted value of the discrimination probability will be P_{disc}=30.7%. The corresponding effective photon counting quantum efficiency will be $\eta_{Q_{eff}}$ = 27.6% at λ=820nm and $\eta_{Q_{eff}}$ = 2.15% at λ=1060nm at a dark count rate of less than 10,000/sec. This photon counter, if built, will clearly be superior to any PMT and APD in analog mode at the wavelength range.

References

[1] J. A. Reagan, M. P. McCormick, and J. D. Spinhirne, 'Lidar sensing of aerosols and clouds in the troposphere and stratosphere,' *Proceedings of the IEEE*, Vol. 77, No. 3, pp. 433-448, March 1989.

[2] R. J. Curran, 'Satellite-borne lidar observations of the earth: Requirements and anticipated capabilities,' *Proceedings of the IEEE*, Vol. 77, No. 3, pp. 478-490, March 1989.

[3] J. L. Bufton, 'Laser altimetry measurements from aircraft and spacecraft,' *Proceedings of the IEEE*, Vol. 77, No. 3, pp. 449-462, March 1989.

[4] 'High speed solid state detectors for fiber optic and very low light-level applications,' RCA Inc., Electro Optics, Silicon avalanche photodiodes C30902E, C30902S, C30921E, C30921S (data sheet), 1988.

[5] *Photomultiplier Tubes*, Hamamatsu Corporation, Catalog, 1989, p. 77.

[6] K. Kikuchi, T. Okoshi, and A. Hirose, 'Achievement of shot-noise-limited sensitivity and 50 dB dynamic range by photon-counting receiver using Si avalanche photodiode,' *Electronics Letters*, Vol. 21, No. 18, pp. 801-802, Aug. 1985.

[7] A. W. Lightstone and R. J. McIntyre, 'Photon counting silicon avalanche photodiodes for photon correlation spectroscopy,' *Proceedings of the OSA topical Meeting on Photon Correlation Techniques and Applications*, May 31-June 2, 1988, Washington, DC, pp. 183-191.

[8] P. P. Webb, R. J. McIntyre, and J. Conradi, 'Properties of avalanche photodiodes,' *RCA Review*, Vol. 35, pp. 234-278, June 1974.

[9] T. V. Muoi, 'Receiver design for digital fiber optic transmission systems using Manchester (biphase) coding,' *IEEE Trans. Commun.*, Vol. COM-31, No. 5, pp. 608-619, May 1983.

[10] J. B. Abshire, 'Performance of OOK and low-order PPM modulations in optical communications when using APD-based receivers,' *IEEE Trans. Commun.*, Vol. COM-32, No. 10, pp. 1140-1143, Oct. 1984.

[11] R. G. Smith and S. D. Personick, 'Receiver design for optical fiber communication systems,' in *Semiconductor Devices for Optical Communications*, H. Kressel ed., Springer-Verlag, New York, 1980, ch. 4.

[12] F. M. Davidson and X. Sun, 'Gaussian approximation versus nearly exact performance analysis of optical communication systems with PPM signaling and APD receivers,' *IEEE Trans. Commun.*, Vol. COM-36, No. 11, pp. 1185-1192, Nov. 1988.

[13] X. Sun, *Free-Space Direct-Detection Optical Communication with Semiconductor Laser Transmitters and Avalanche Photodiode Photodetectors*, Ph.D thesis, the Johns Hopkins University, Baltimore, MD, 1989.

[14] T. E. Ingerson, R. J. Kearney, and R. L. Coulter, 'Photon counting with photodiodes,' *Applied Optics*, Vol. 22, No. 13, pp. 2013-2018, June 1983.

[15] H. H. Tan, 'Avalanche photodiode statistics in triggered-avalanche detection mode,' TDA Progress Report 42-79 (N85-13987), pp. 69-80, July-September 1984.

[16] P. G. W. Brown, K. D. Ridley, and J. G. Rarity, 'Characterization of silicon avalanche photodiodes for photon correlation measurements. 1: Passive quenching,' *Applied Optics*, Vol. 25, No. 22, pp. 4122-4126, Nov. 1986.

[17] P. G. W. Brown, R. Jones, J. G. Rarity, and K. D. Ridley, 'Characterization of silicon avalanche photodiodes for photon correlation measurements. 2: Active quenching,' *Applied Optics*, Vol. 26, No. 12, pp. 2383-2389, June 1987.

[18] B. I. Cantor and M. C. Teich, 'Dead-time-corrected photocounting distributions for laser radiation,' *Journal of the Optical Society of America*, Vol. 65, No. 7, pp. 786-791, July 1975.

[19] D. L. Snyder, *Random Point Processes*, John Wiley & Sons, New York, 1975, p. 252.

[20] R. J. McIntyre, 'The Distribution of gains in uniformly multiplying avalanche photodiodes: Theory,' *IEEE Trans. Electron Devices*, Vol. ED-19, No. 6, pp. 703-713, June 1972.

[21] J. Conradi, 'The Distribution of gains in uniformly multiplying avalanche photodiodes: Experimental,' *IEEE Trans. Electron Devices*, Vol. ED-19, No. 6, pp. 713-718, June 1972.

[22] M. L. Skolnik, *Introduction to Radar Systems*, McGraw-Hill, New York, 1962, p. 31.

[23] P. Horowitz and W. Hill, *The Art of Electronics*, Cambridge, New York, 1980, p. 306.

[24] *GigaBit Logic 1991 GaAs IC Data Book & Designer's Guide*, GigaBit Logic Inc., Newbury Park, CA, August 1990.

[25] A. D. MacGregor, B. Dion, C. Noldeke, and O. Duchmann, '39 photons/bit direct detection receiver at 810 nm, BER = 1×10^{-6}, 60 Mb/s QPPM,' *Free-Space Laser Communication Technologies III*, David L. Begley and Bernard D. Seery, editors, proc. SPIE 1417-52, 1991.

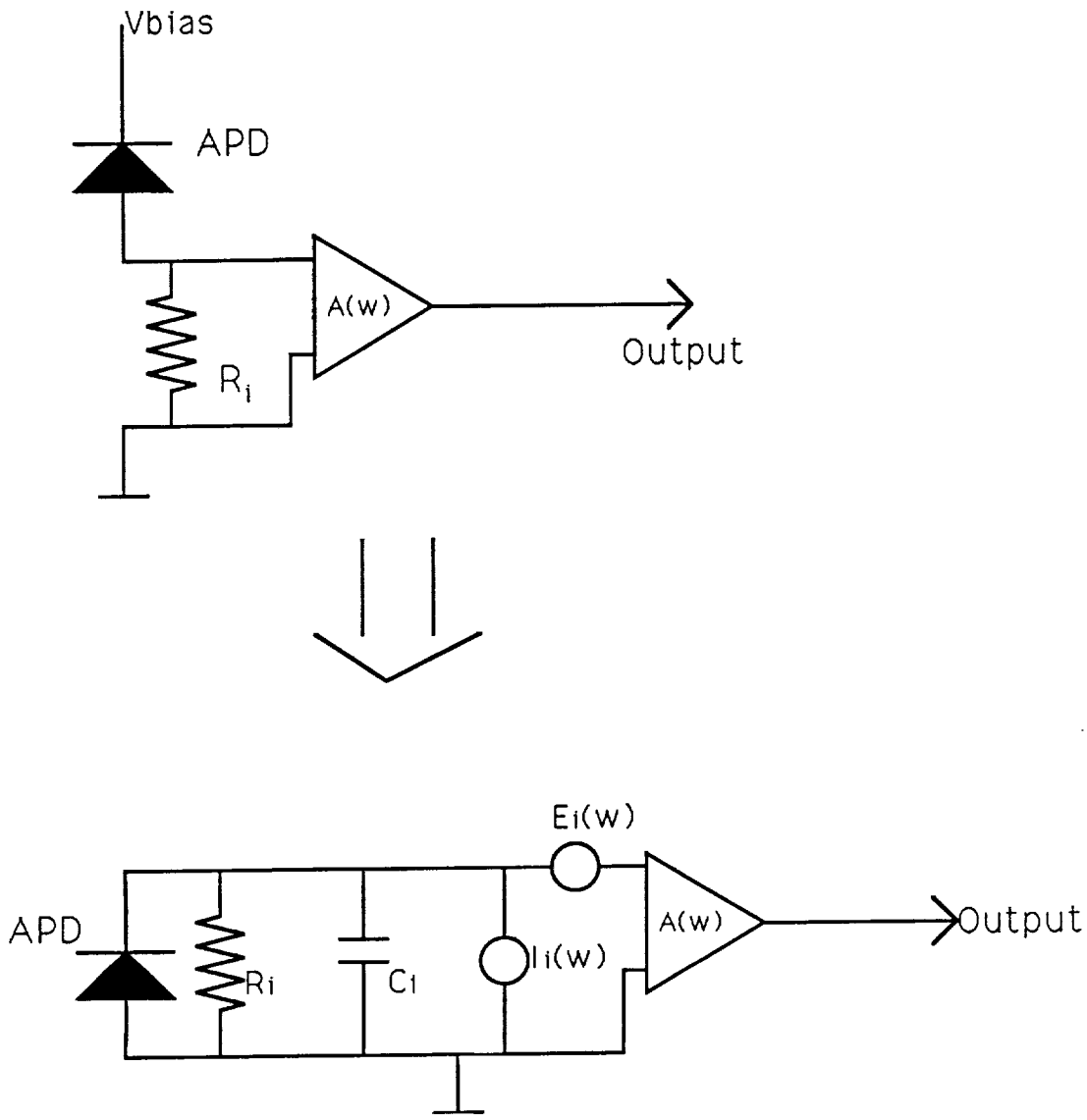

Figure 1. High input impedance APD preamplifier.

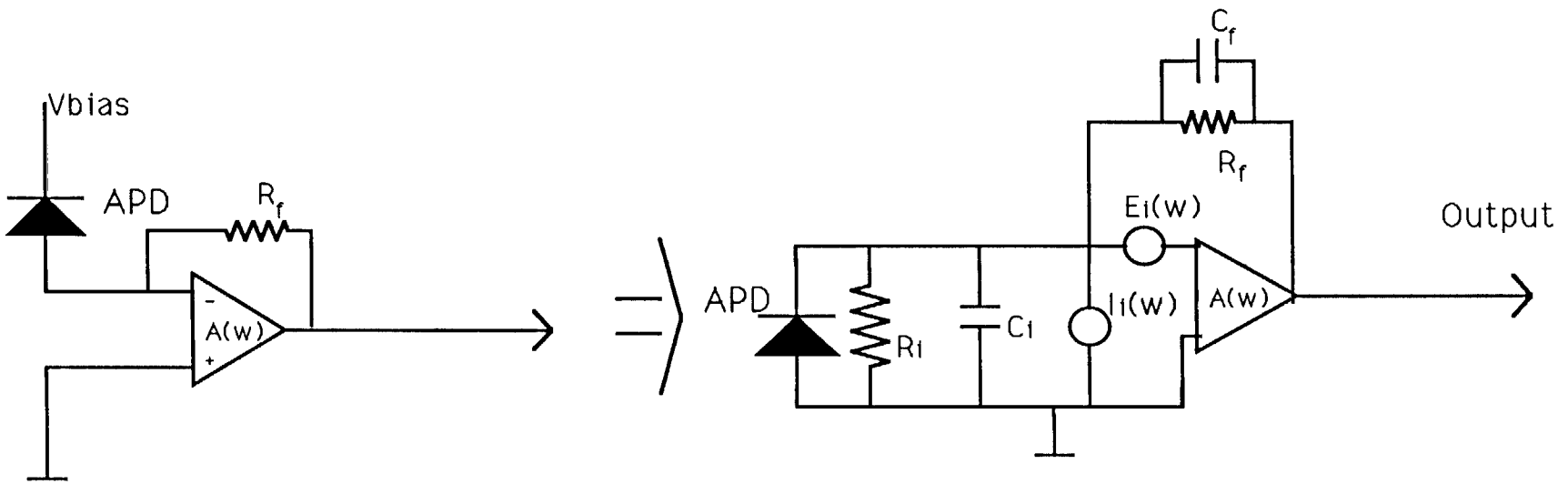

Figure 2. Transimpedance APD preamplifier.

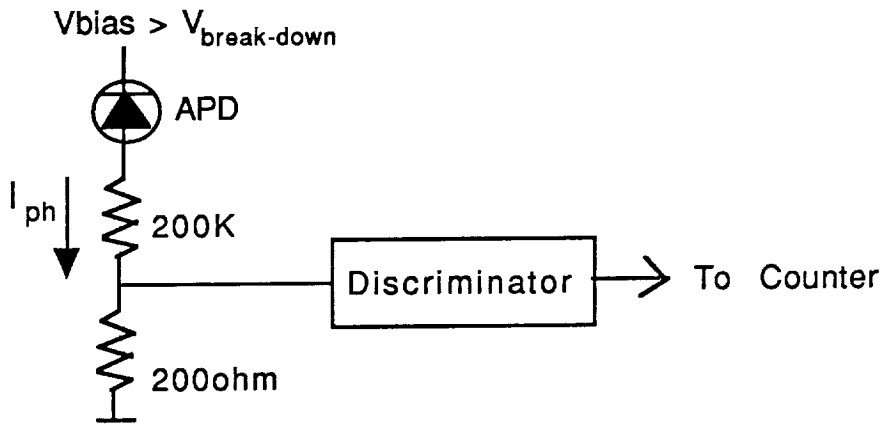

Figuire 3. Avalanche break-down APD photon counter.

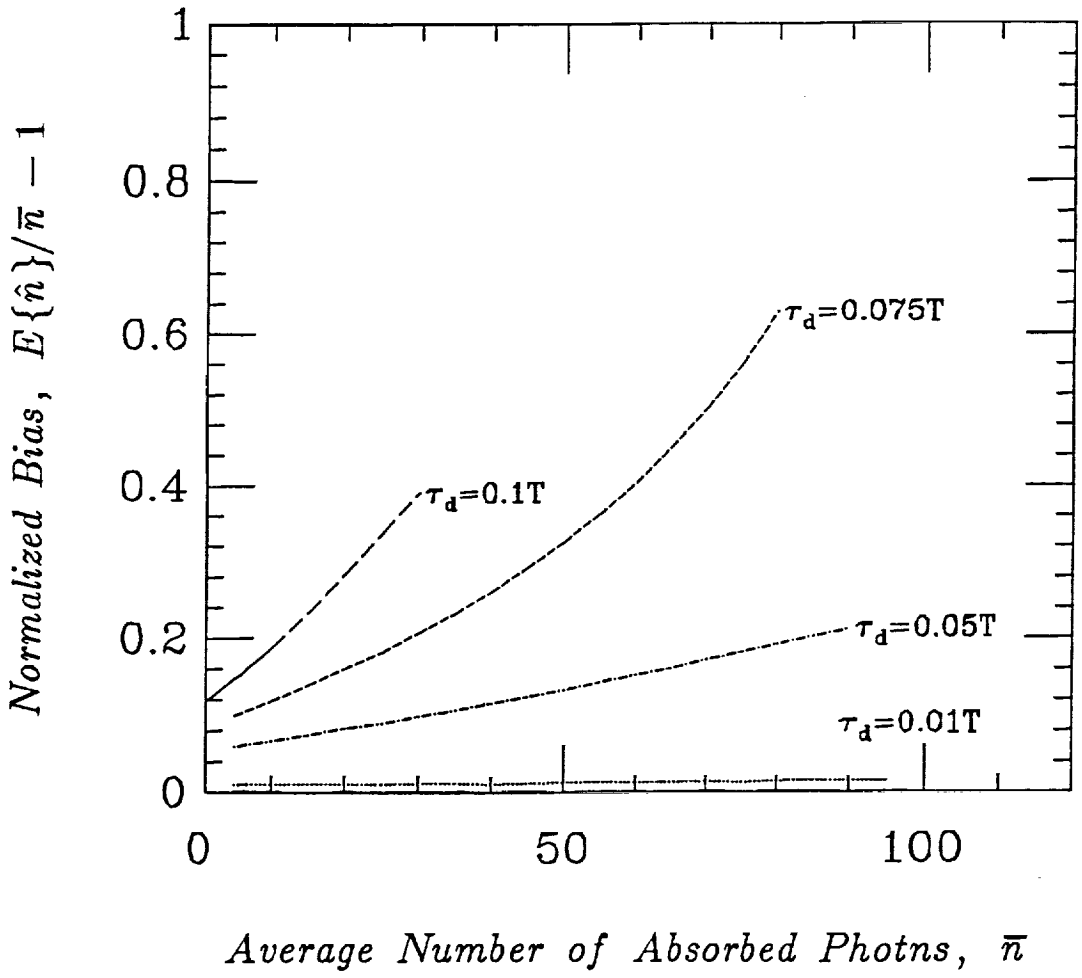

Figure 4. Normalized bias of the ML estimator, $E\{\hat{n}\}$, as a function of the average number of absorbed photons, $\bar{n}$.

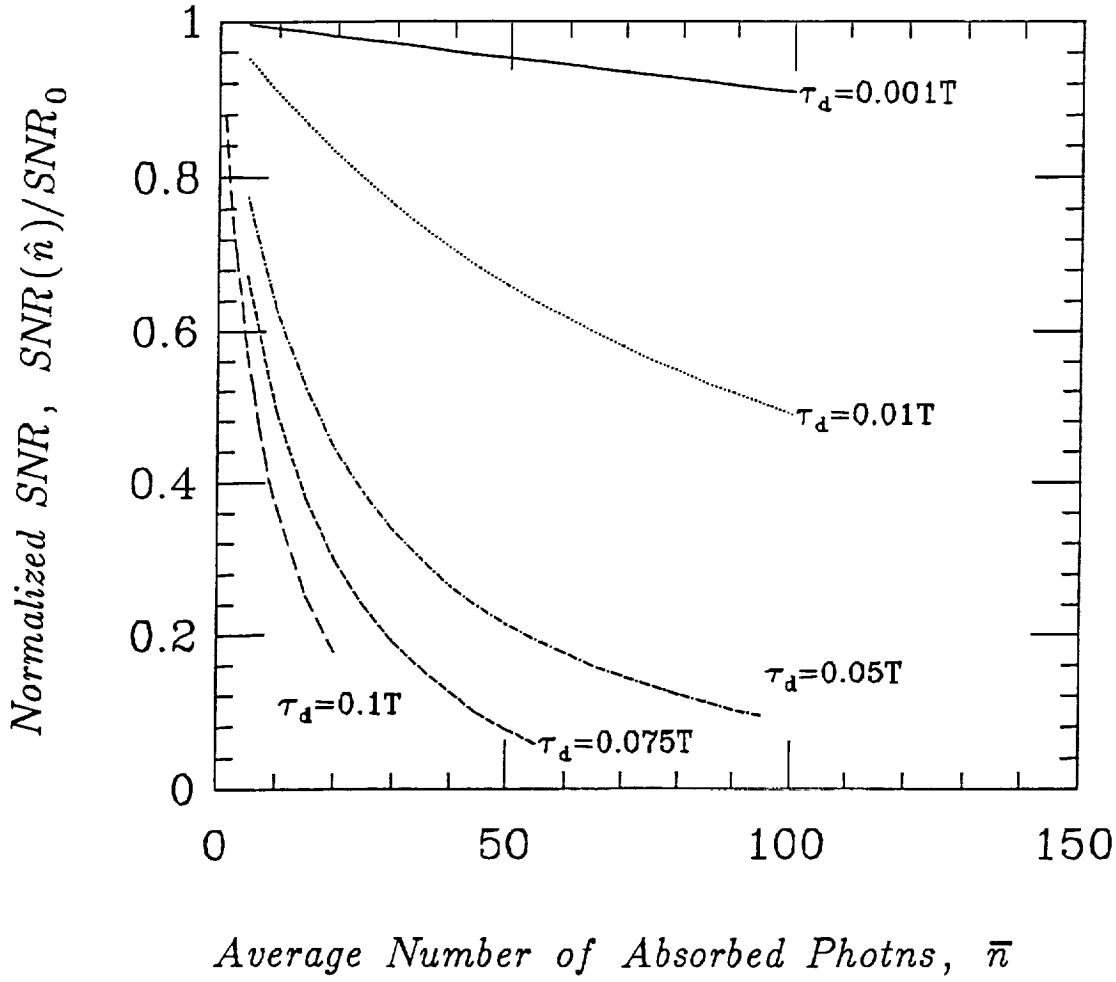

Figure 5. Normalized SNR of the ML estimator $SNR(\hat{n})$ as a function of the average number of absorbed photons, $\overline{n}$. for a given dead time of τ_d and a counting interval of T seconds.

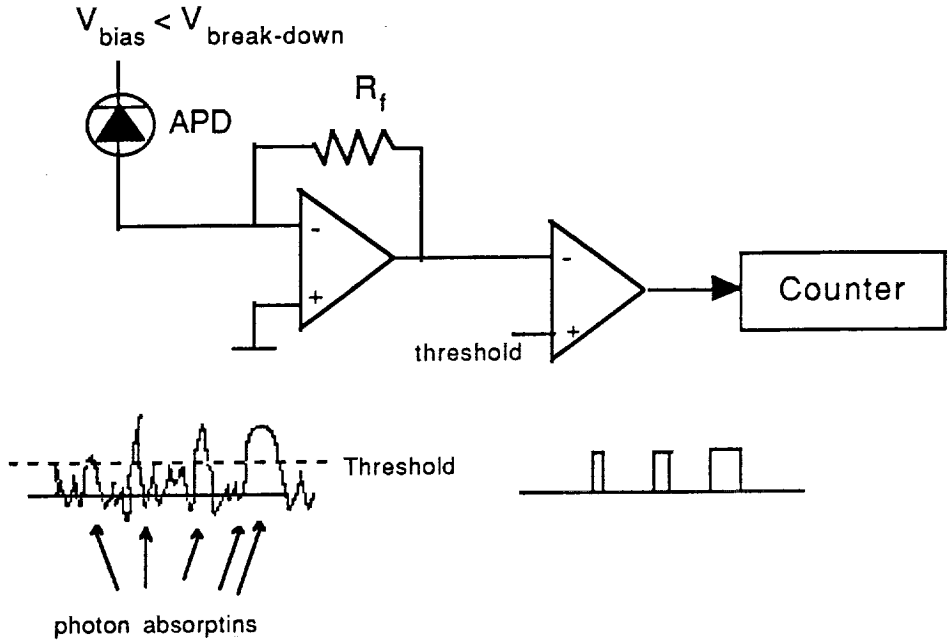

Figure 6. Circuit diagram of nonbreak-down APD photon counter.

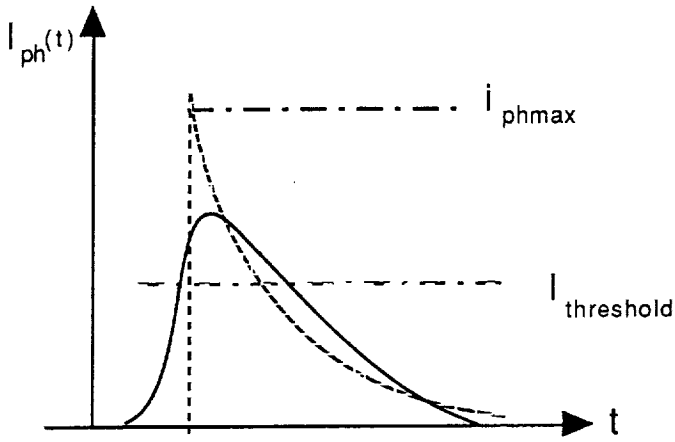

Figure 7. Photocurrent pulse shape. The dashed line represents the ideal exponential pulseshape and the solid line represents a more realistic pulseshape.

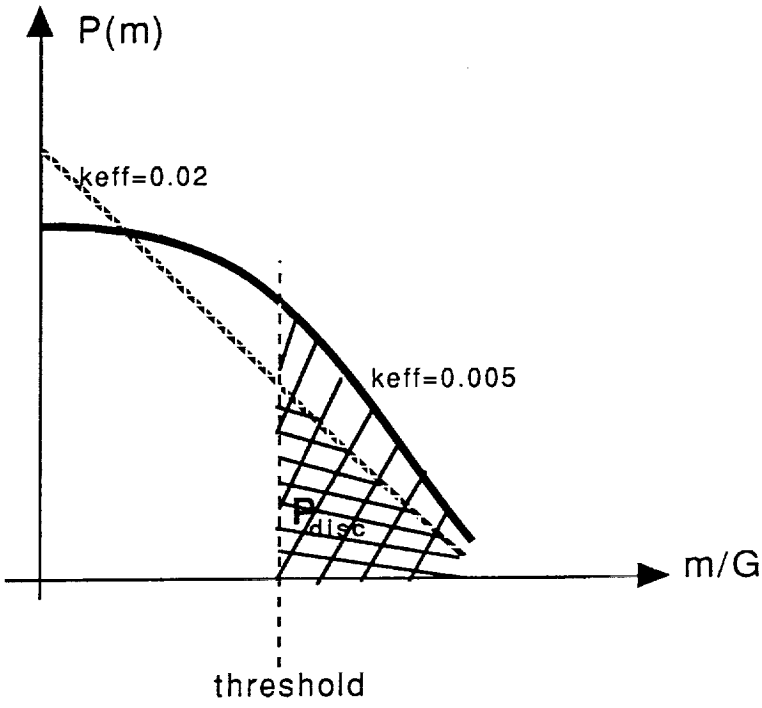

Figure 8. Probability of APD gain.

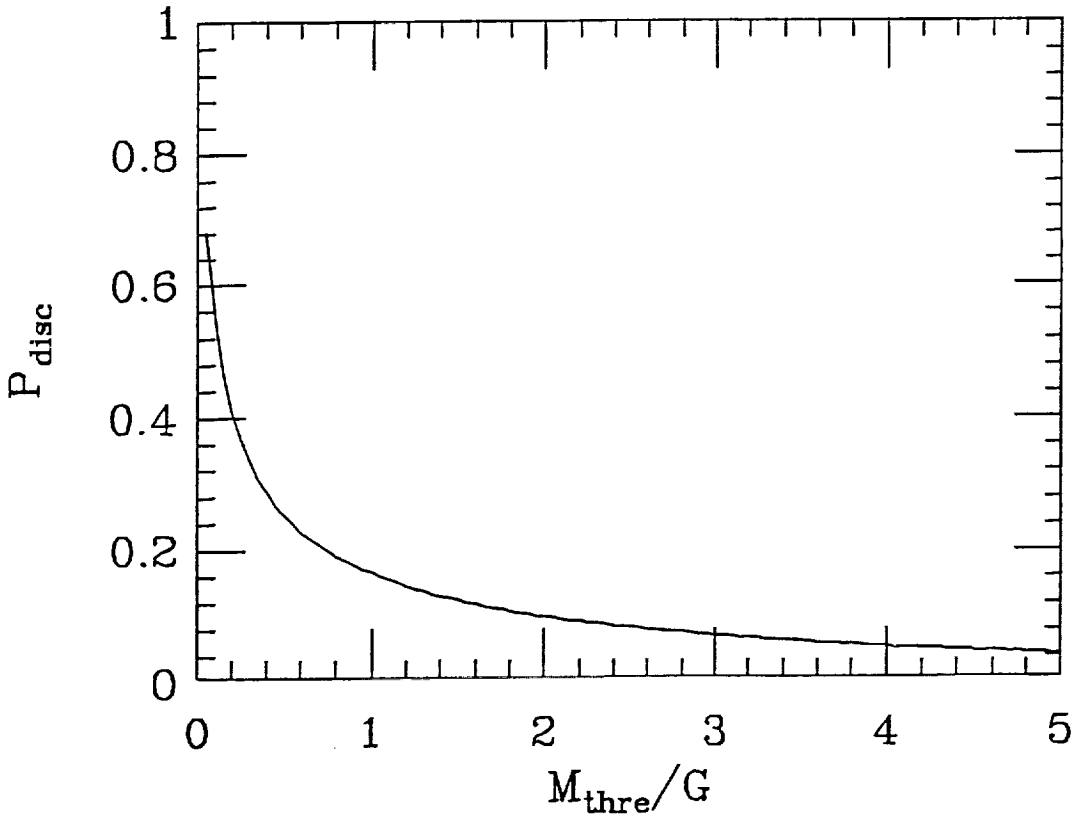

Figure 9. Probability of discrimination, P_{disc}, of a nonbreak-down APD photon counter versus the equivalent threshold gain, M_{thre}.

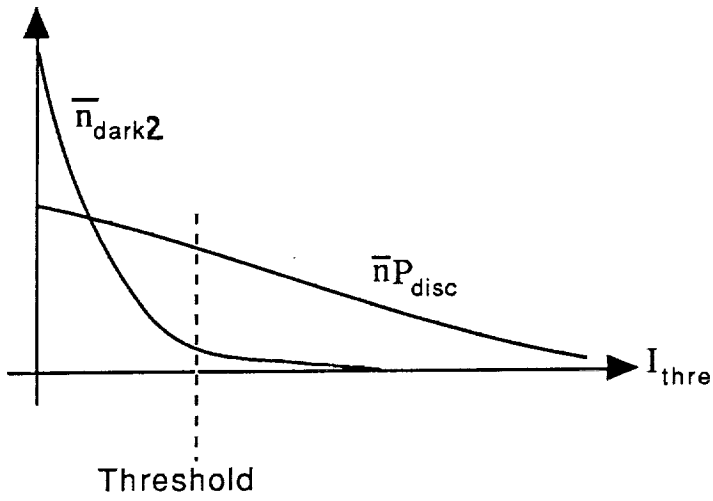

Figuire 10. Average numbers of detected photons and dark counts as a function of the threshold.

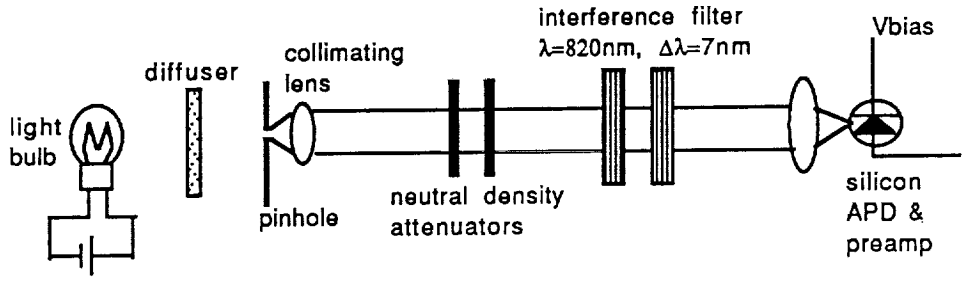

Figure 11. Optical Setup of the Experiment.

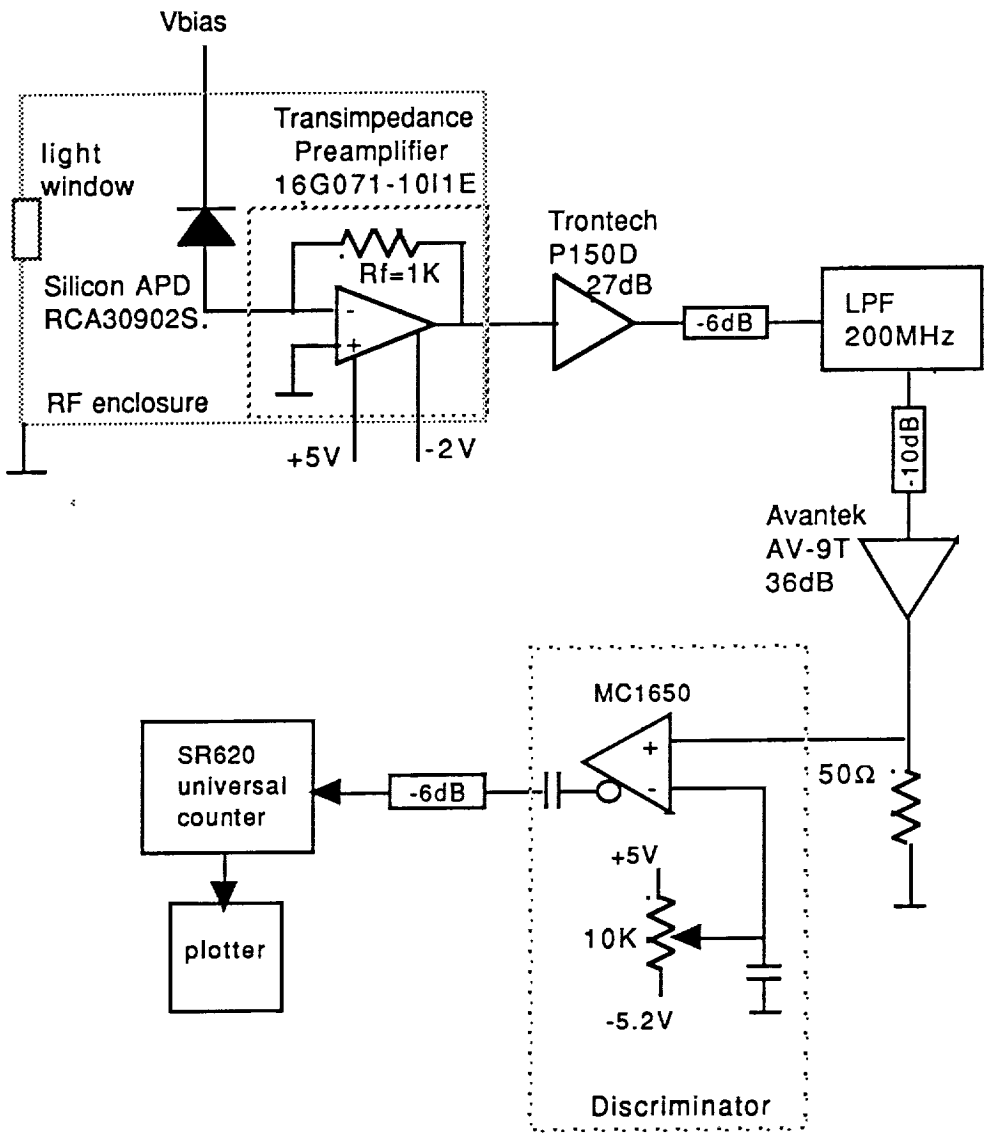

Figure 12. Non break-down APD photon counter circuit.

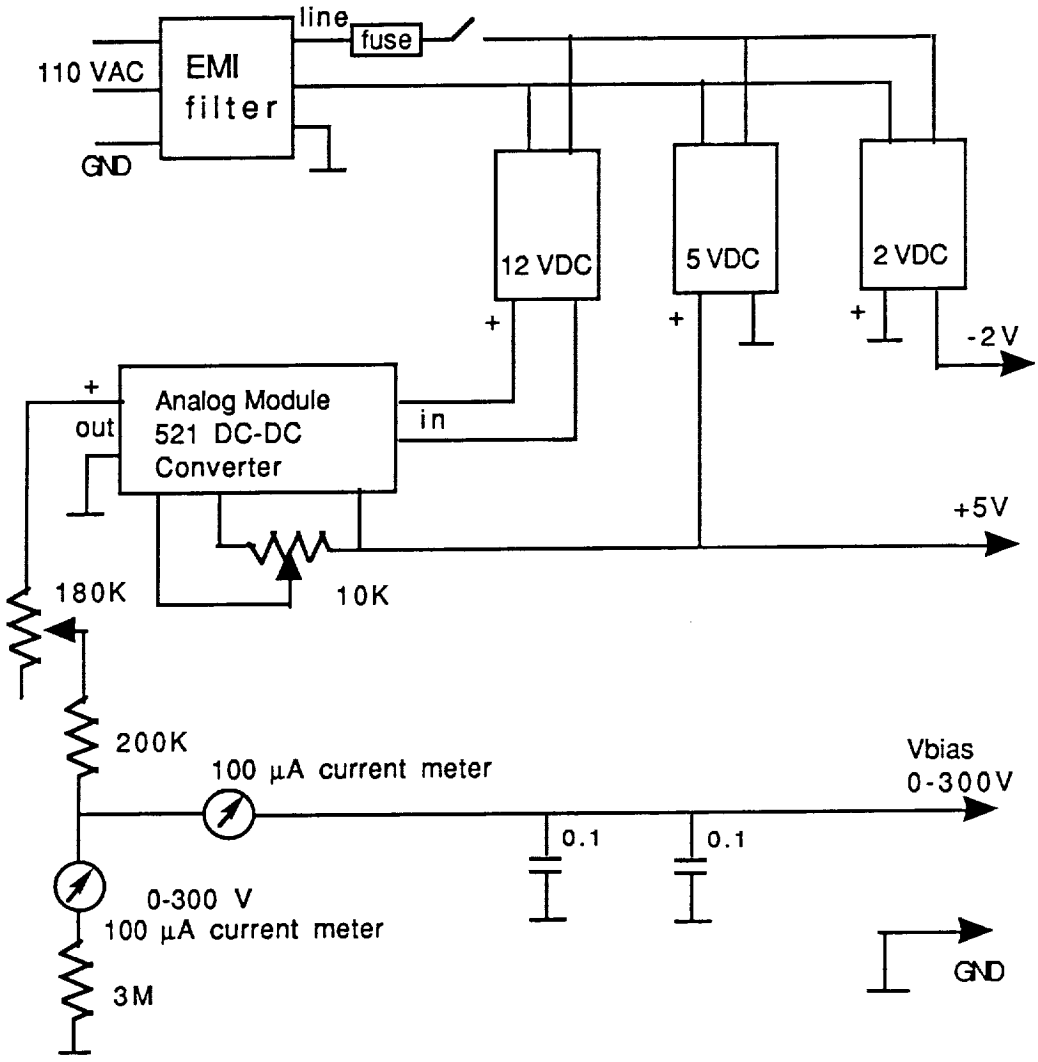

Figure 13. APD/Preamp DC supply.

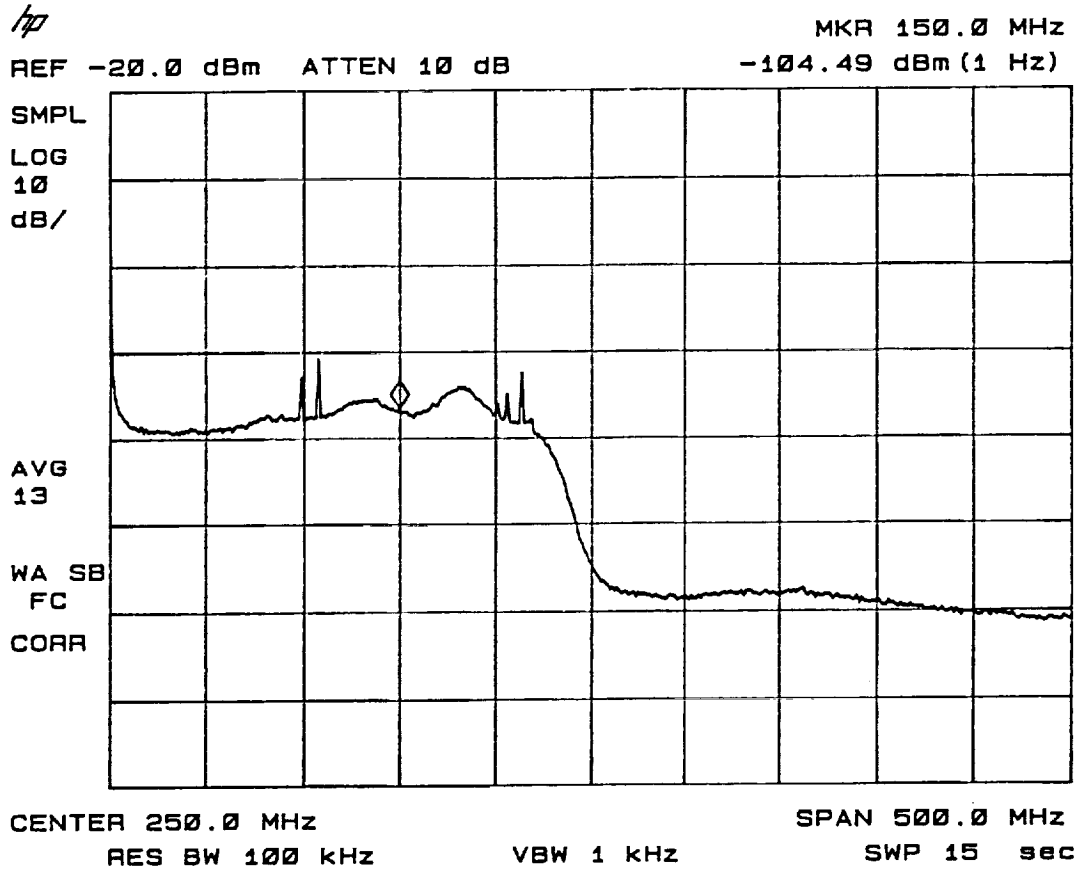

Figure 14. Power spectrum of the total circuit thermal noise measured at the input of the comparator.

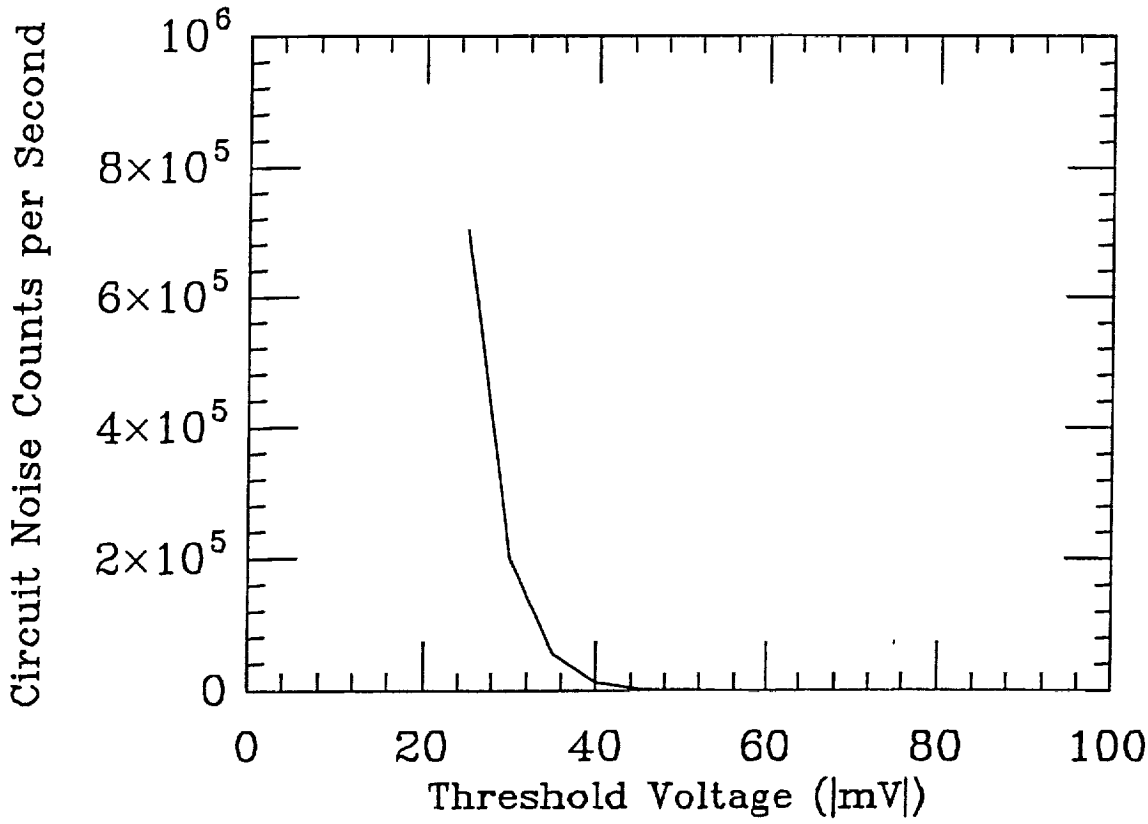

Figure 15. Circuit thermal noise counts versus threshold voltage applied at the comparator.

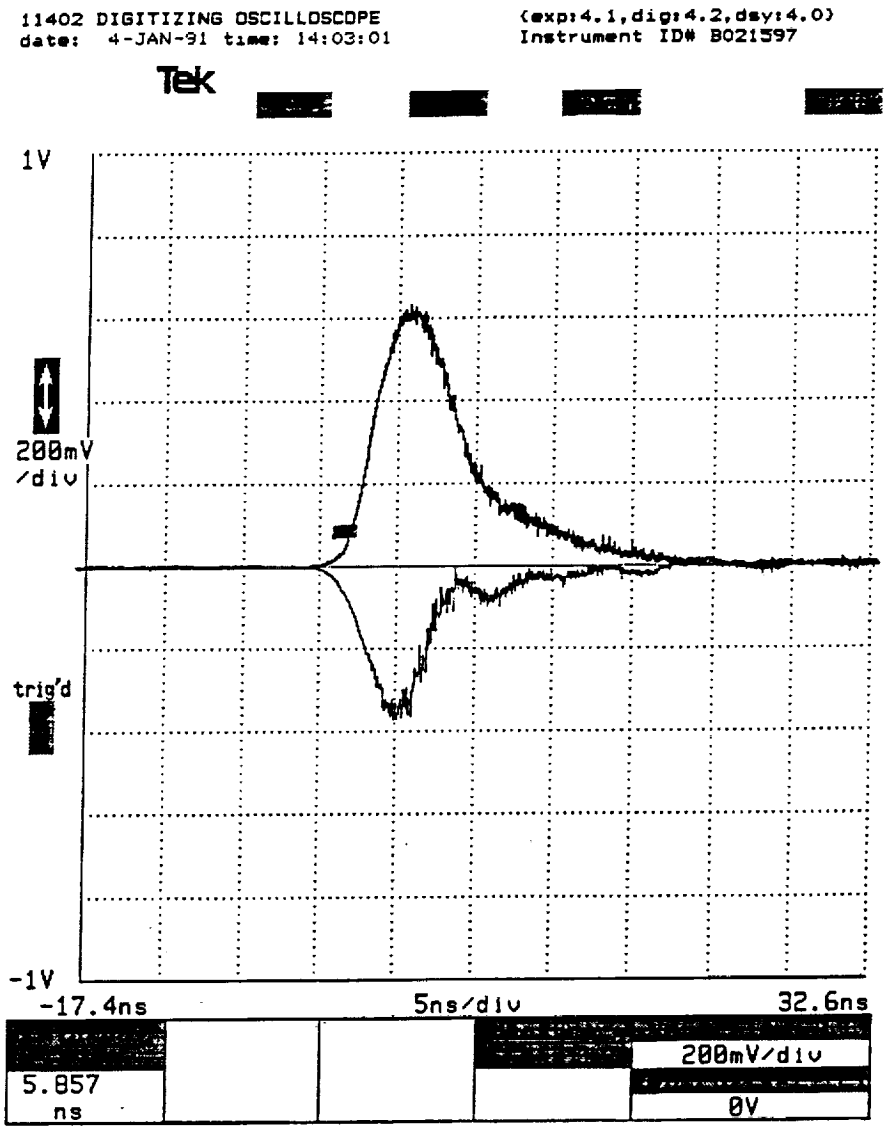

Figure 16. Average waveforms of input pulses (negative going) and output pulses (positive going) of the comparator.

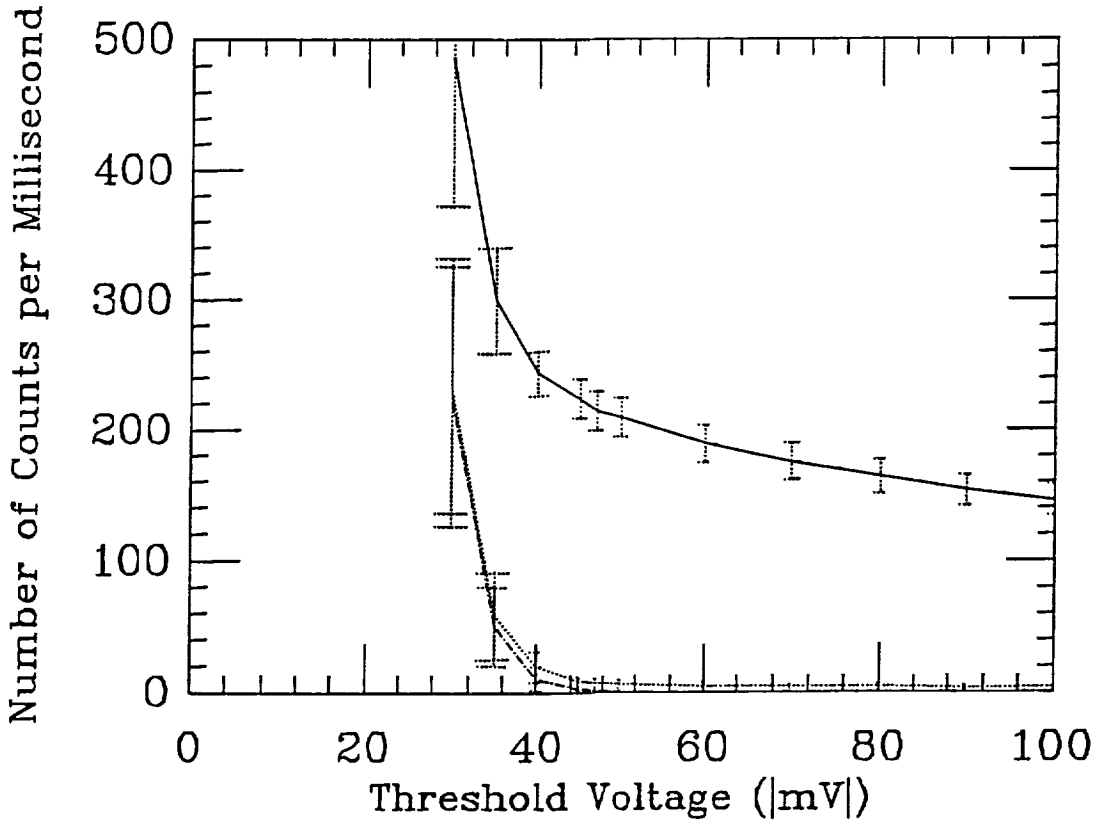

Figure 17. Average number and standard deviation (solid curve) of the detected counts in 1 ms under 1 pW received optical power as a function of the threshold voltage applied at the comparator. The dot-dashed and the dotted curves represent the circuit thermal noise counts (APG gain G=0) and the total dark counts (G~1000), respectively.

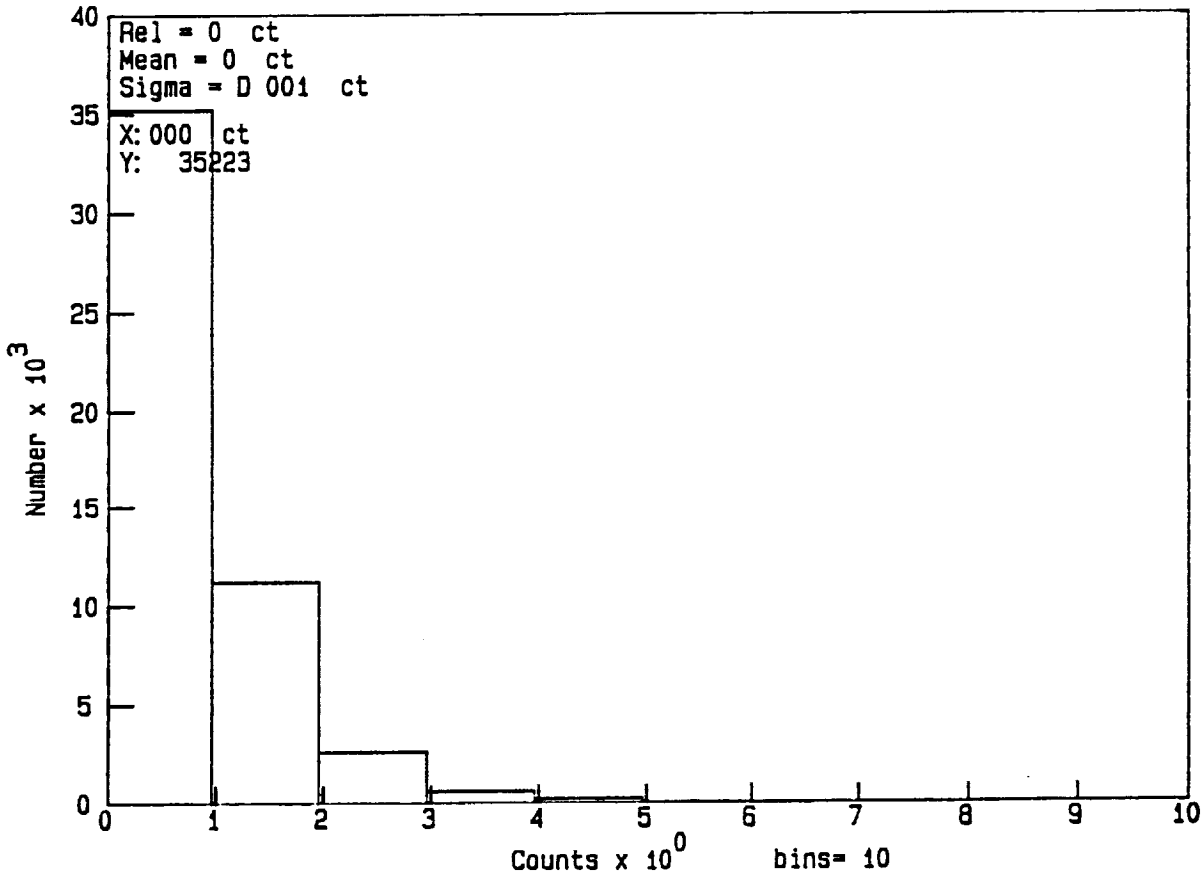

Figure 18. Histogram of circuit thermal noise noise counts over a 1 ms counting interval. The sample size was 5×10^4.

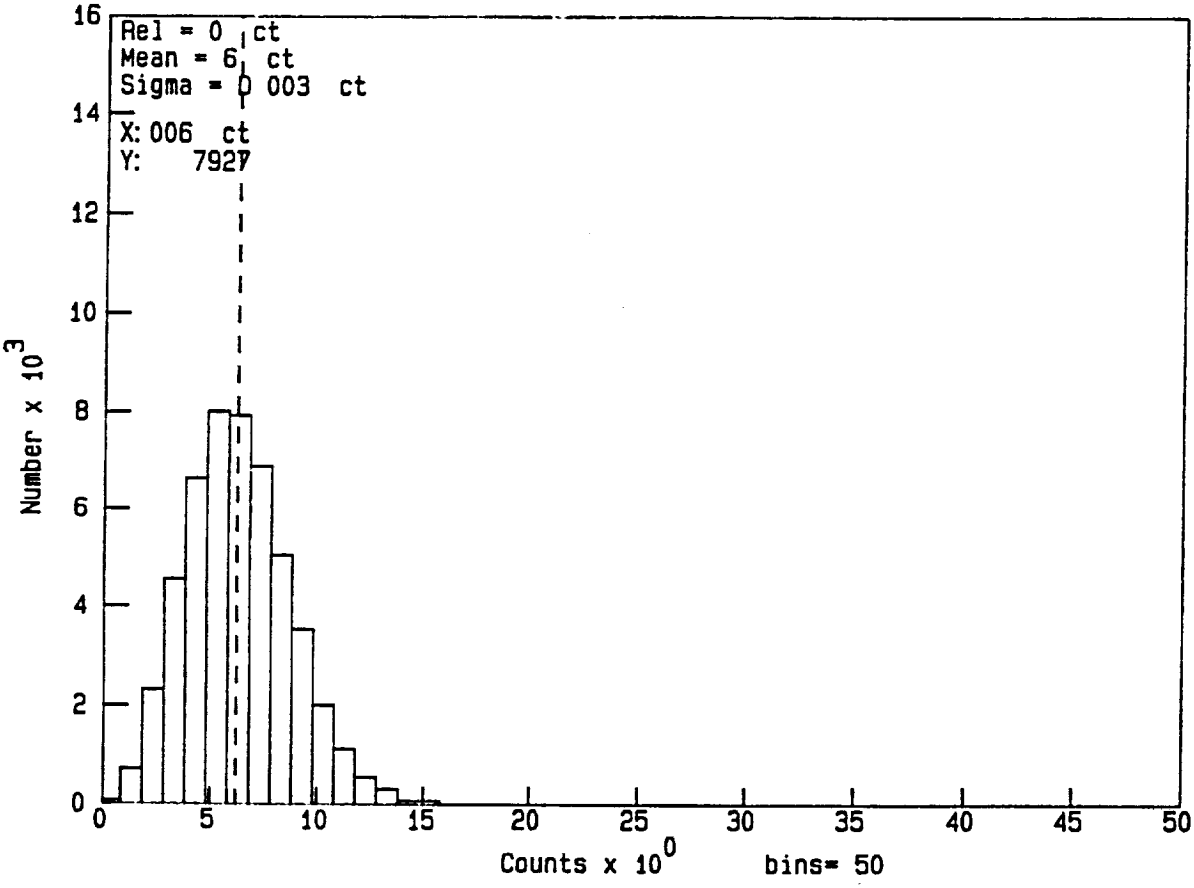

Figure 19. Histogram of the number of the total measured dark counts over a 1 ms counting interval. The sample size was 5×10^4.

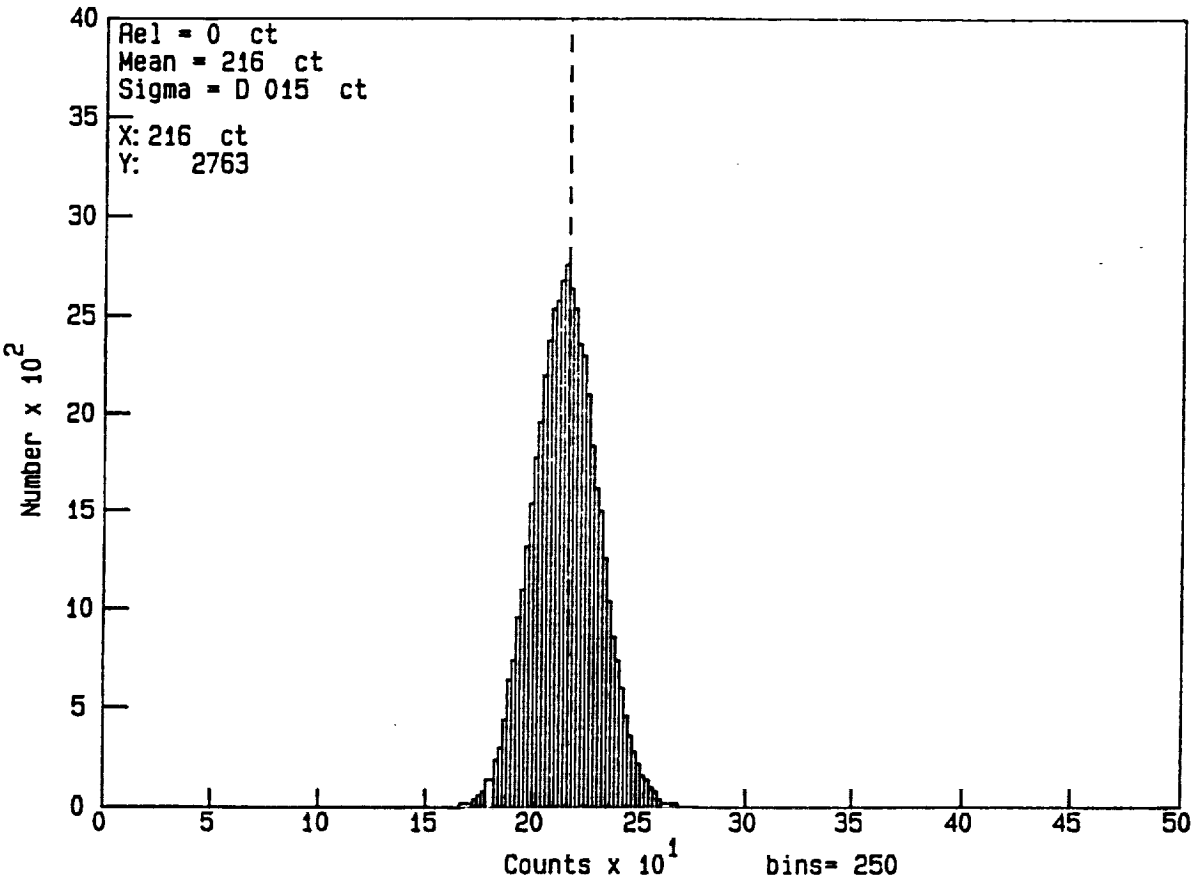

Figure 20. Histogram of the number of the detected counts under 1 pW received optical power over a 1 ms counting interval. The sample size was 5×10^4.

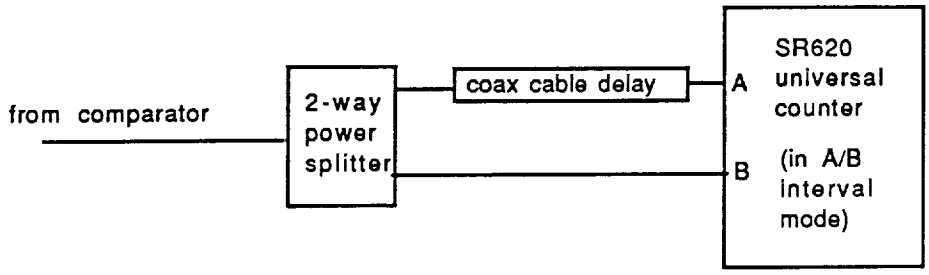

Figure 21. Apparatus used for measuring interarrival times.

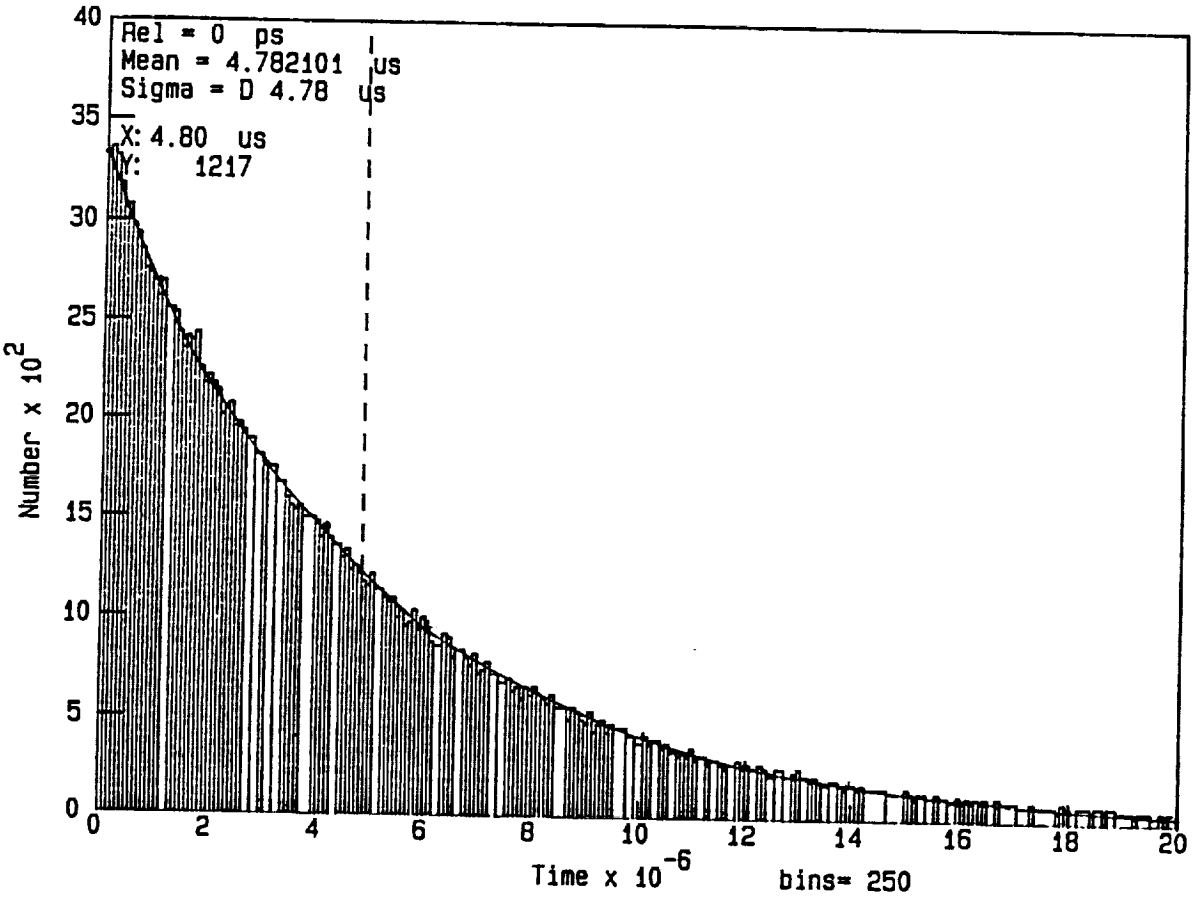

Figure 22. Histogram of the interarrival times under 1 pW received optical power. The solid curve corresponds to the exponential distribution with the same mean (i.e. $3308 exp\,[-t/4.78\times10^{-6}]$). The sample size was 2×10^5.

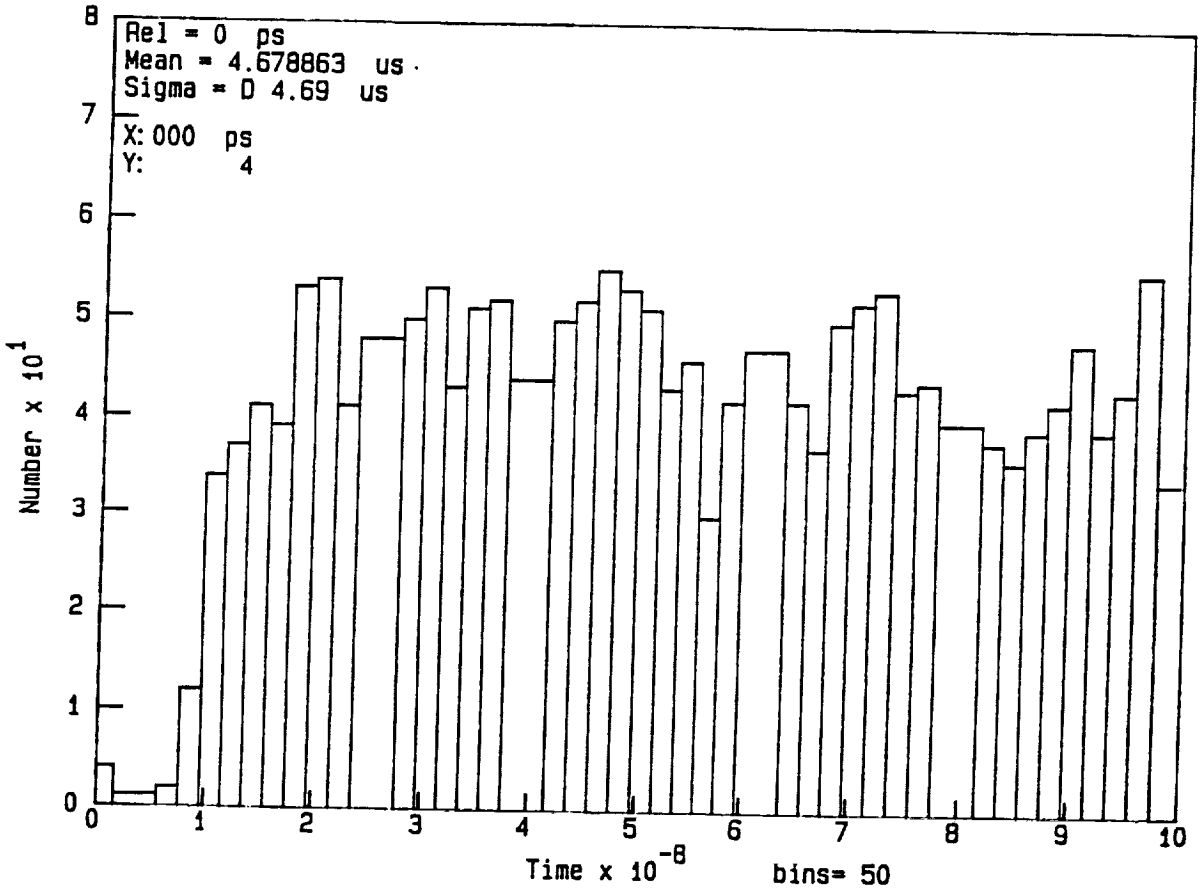

Figure 23. Same as Figure 22 but over an interarrival time from 0 to 100 ns.

Table 1. Measured counts versus received optical power.

P(pW)	cts/ms	σ	var/mean*	η**	η_{corr}***
0.0	6	3	1.00	N/A	N/A
0.1	28	6	1.18	5.1%	5.1%
0.3	69	8	0.88	5.0%	5.0%
1.0	216	15	1.02	5.2%	5.2%
3.0	629	26	1.07	5.1%	5.1%
10	1990	43	0.93	4.8%	5.0%
30	5270	72	0.98	4.2%	4.6%
40	6510	87	1.16	3.9%	4.3%
50	7500	99	1.31	3.6%	4.1%
60	8670	107	1.32	3.5%	4.0%
70	9630	127	1.67	3.3%	3.9%
100	12.3×10^3	153	1.91	3.0%	3.6%
200	17.7×10^3	214	2.58	2.1%	2.9%
300	20.7×10^3	261	3.28	1.7%	2.4%
400	22.7×10^3	294	3.80	1.4%	2.1%
500	24.7×10^3	232	2.18	1.2%	1.9%

* var/mean $= (\sigma^2-\sigma^2_{ther})/(mean-mean_{ther})$ with the mean and the standard deviation of the circuit thermal noise counts, $mean_{ther}$=1 and σ_{ther}=2, respectively.

** $\eta=(mean-mean_{dark})/(P_{in}\,T/hf\,)$ with the counting interval, T=1ms, the received optical power, P_{in}= 1.0 pW, and the photon energy, hf =1.51eV.

*** $\eta_{corrected}=\eta/[1-(\tau_d/T)\bar{n}_c]$ with τ_d the dead time (15ns) and $\bar{n}_c$ the average number of observed counts.

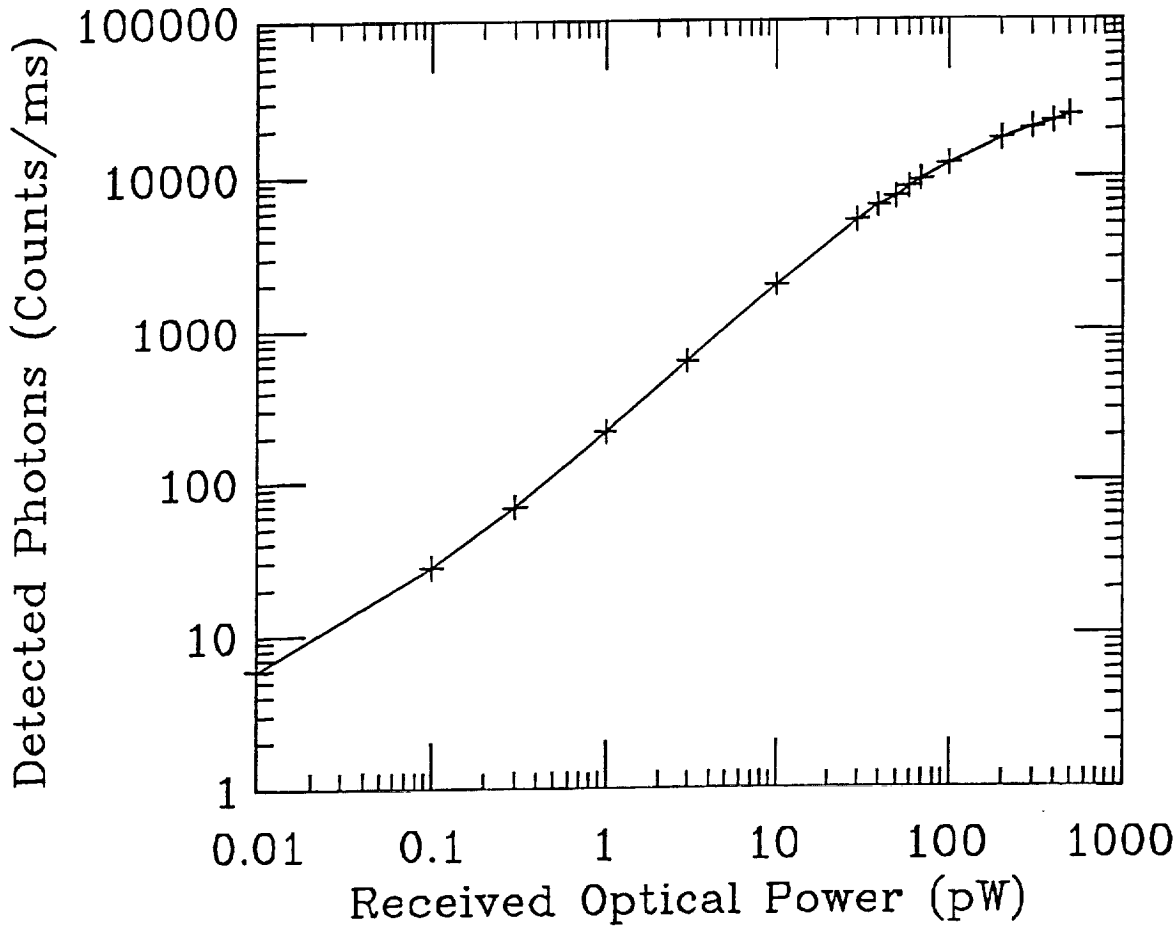

Figure 24. Average number of detected counts of the experimental nonbreakdown APD photon counter versus received optical power in pW.